KineCluE a Kinetic Cluster Expansion code to compute transport coefficients beyond the dilute limit

T. Schuler, L. Messina, M. Nastar

▶ **To cite this version:**

KineCluE: a Kinetic Cluster Expansion code to compute transport coefficients beyond the dilute limit

Thomas Schuler[a,b,*], Luca Messina[a], Maylise Nastar[a]

[a]*DEN-Service de Recherches de Métallurgie Physique, CEA, Université Paris-Saclay, F-91191 Gif-sur-Yvette, France*
[b]*Mines Saint-Etienne, Univ Lyon, CNRS, UMR 5307 LGF, Centre SMS, F-42023 Saint-Etienne, France*

Abstract

This paper introduces the KineCluE code that implements the self-consistent mean-field theory for clusters of finite size. The transport coefficients of a system are then obtained as a sum over cluster contributions (cluster expansion formalism), each being individually obtained with KineCluE. This method allows to go beyond the infinitely dilute limit and is an important step in bridging the gap between dilute and concentrated approaches. Inside a finite volume of space containing the components of a single cluster, all kinetic trajectories are accounted for in an exact manner. The code, written in Python, adapts to a wide variety of systems, with various crystallographic systems (eventually strained), defects and solute types and number, and various jump mechanisms, including collective ones. The code also features interesting tools such as the sensitivity study routine which allows to identify the most important jump frequencies to get accurate transport coefficients.

Keywords: Phenomenological coefficients, Coarse graining, Diffusion, Cluster expansion, Alloy kinetics, Random walk

PROGRAM SUMMARY

Program Title: KineCluE (KINEtic CLUster Expansion)

Licensing provisions: LGPL
Programming language: Python 3.6

Nature of problem: Providing a general method for computing transport coefficients from atomic jump frequencies, taking into account kinetic correlations.

Solution method: The program relies on the self-consistent mean field theory. The system is described in terms of lattice sites, defects and jump mechanisms. The first part of the code translates the diffusion problem for such system into an analytical linear eigenvalue problem. The second part of the code assigns numerical values to each analytical variable and then solves the linear problem.

1. Introduction

Atomic transport in solids has attracted enormous experimental[1] and theoretical[2, 3] attention over the past 70 years. It is still a challenging problem in various ways. In the first place, the microscopic dynamical rules determining the macroscopic diffusion coefficients are becoming more and more complex as the investigations based on the density functional theory (DFT)[4] provide an increasingly detailed description of the atomic transport mechanisms [5–7]. In addition, the effort of solving the N-body problem of N interacting species diffusing on a lattice has been mainly focused on the limiting case of two-body diffusion problems both in dilute [3] and–with simplifying assumptions–concentrated alloys [8–13]. Three-body diffusion problems have only been tackled in very simple systems[14, 15]. Besides, the experimental characterization of atomic transport at low temperature is

---

[*]Corresponding author.
E-mail address: thomas.schuler@cea.fr

in general not feasible, and only some of the transport coefficients can be experimentally determined. Thanks to the progress of DFT applied to the calculation of migration barriers [16–18], atom jump frequency databases are in construction for metallic alloys [6, 19–22], but also for ceramics [23, 24] and semi-conductors [25–29]. The use of these databases is mainly dedicated to the study of self- and solute diffusion [19, 21]. Much less attention has been paid to the estimation of the full Onsager matrix [30], although the latter is essential to investigate flux coupling between point defects and atomic species occurring in systems driven by a supersaturation of point defects, in materials submitted to irradiation [31, 32] as well as during thermal quenching treatments [33] or under severe plastic deformation [34].

In most cases, diffusion mechanisms in solids are mediated by point defects, the most frequent ones being the exchange of an atom with a first nearest neighbor (1NN) vacancy (a vacant site of the lattice) and the exchange of an atom with a 1NN self-interstitial. One of the most stable interstitial configuration is the dumbbell (or split-interstitial) configuration: a directional pair of atoms sharing a lattice site. This is a complex mechanism possibly leading to a modification of the initial dumbbell composition and direction, and there is still no exact calculation of the associated transport coefficients even in the limiting case of an infinite dilute alloy (a single point defect and solute atom in a host matrix) [11, 35–37]. Due to the small concentration of point defects, the successive jumps of a given atom are correlated because the probability of making several exchanges with the same point defect is larger than the probability of making exchanges with different point defects. These kinetic correlations related to the probability of the PD to perform return paths slow down the diffusion of a tracer atom and are the main contributors to the off-diagonal Onsager coefficients L_{AB} between two atomic species A and B. Thus, they determine the sign and the amplitude of flux couplings. In the limiting case of an infinite dilute alloy containing a vacancy, automated computational schemes have allowed to achieve the calculation of transport coefficients for long–range thermodynamic interactions between solute and point defect [6, 22, 38–45]. At the origin of these numerical schemes, there

are new theoretical developments based either on the Self-Consistent Mean Field theory (SCMF) [41] or on a Green function formalism [15, 44–46]. Indeed, even though computing a macroscopic transport coefficient from microscopic jump rates is a well defined problem, many efforts are still needed to find the general solution.

Within a diffusion theory, one describes the evolution of an alloy by means of a microscopic master equation. One starts from a simplified description of the system as a rigid lattice, whose sites are occupied by either atoms or point defects. Transitions from one configuration to another are fixed by the constraints of the jump mechanisms. These transitions determine the evolution of the distribution function, e.g. the probability of every configuration as a function of time. Solving the master equation and computing the time-dependent distribution function involves finding a non-linear eigenvalue problem coupled to the unknown diffusion driving forces, i.e., the gradients of chemical potentials. At first order in the diffusion driving forces and under a stationary condition, the problem becomes a linear eigenvalue problem, the eigenvalues corresponding to the contribution of the kinetic correlations to the Onsager coefficients. An exact solution was obtained only in the particular case of a vacancy-solute cluster in an infinite medium, this by means of a Green function formalism. [45] However, there exists an exact variational formula of the Onsager coefficients. [47, 48] The various diffusion methods provide upper bounds of the phenomenological coefficients and can be compared with each others. [49] Within the SCMF theory, the kinetic correlations are represented by a non-equilibrium effective Hamiltonian. [50] The unknown kinetic interactions of the effective Hamiltonian are assumed to be a linear combination of the chemical potential gradients, leading to a solution in the form of partial differential kinetic equations. [51] A solute-point defect n-body kinetic interaction is related to the kinetic equation of the corresponding n-th moment of the probability distribution function. [50, 52] In a dilute alloy, the n-th moments are assimilated to the ensemble probabilities of the various configurations of the solute-point defect cluster n.[41] The range of a kinetic interaction is directly related to the length of the return

paths of the cluster components. For example, a 1NN pairwise kinetic interaction accounts for point defect two-jump return paths only. A systematic increase of the kinetic interaction range yields the Onsager coefficient as a series converging to the exact Onsager solution of a single cluster in an infinite medium. The use of symmetry operations for the analysis of the point-defect exchange frequencies and the computation of the Onsager coefficients have recently widen the investigations to more complex crystallographic structures, as for example the study of solute drag in strained systems [53] and in the hexagonal close packed magnesium crystal [43]. However, we still miss a kinetic method that can handle complex diffusion mechanisms among which are the dumbbell diffusion mechanism [36], the kick-out mechanism [54], the macro-jumps of two-half vacancies surrounding a large-sized solute atom [55]. In these cases, the challenge is to achieve a full exploration of the configuration phase space, use symmetry operations to reduce the configuration phase space, then build a graph whose vertices represent the configurations and edges represent the authorized transitions. Moreover, a systematic method dealing with larger clusters than a two-body clusters does not exist yet.

We introduce KineCluE, an automated code dedicated to dilute alloys with intermediate solute concentrations between the infinite dilute and concentrated limits. Recently, we have derived an approximation scheme based on a division of the system into point defect-solute cluster sub-spaces [41, 56]. Computing separately the transport coefficient contribution of each cluster considered isolated in an infinite medium and then modeling the system as a lattice gas of clusters leads to a very efficient approach of diffusion and phase transformations in dilute systems. Within this new formalism, the total Onsager matrix is split into intrinsic cluster Onsager matrices, allowing as well for a proper definition of the cluster mobility and dissociation rate. The code is versatile and able to deal with many types of crystal structures, defect types and jump mechanisms, including collective ones. Its ability to perform calculations on clusters larger than pairs is an important step in bridging the gap between dilute and concentrated approaches of diffusion problems. Section 2 presents the theoretical framework behind KineCluE. Then, the tech-

nical implementation of the code is described in Sec. 3, and some examples of results obtained with the code are presented in Sec. 4.

2. Theoretical background

2.1. Cluster transport coefficients

Transport coefficients appear in the framework of the thermodynamics of irreversible processes, originally developed by Onsager [30, 57]:

$$\vec{J}_\alpha = -\sum_\beta L_{\alpha\beta} \vec{\nabla} \frac{\mu_\beta}{k_B T}, \quad (1)$$

where $L_{\alpha\beta}$ is the Onsager transport coefficient (units of $\left[\mathrm{m^{-1}s^{-1}}\right]$) relating the flux $\vec{J}_\alpha$ of species α under a chemical potential gradient $\vec{\nabla}\mu_\beta$ of species β, k_B is the Boltzmann constant, T is the absolute temperature. The Allnatt formula relates the transport coefficients with equilibrium fluctuations of atomic positions [58]:

$$L_{\alpha\beta} = \lim_{\tau \to \infty} \frac{\left\langle \Delta \vec{R}_\alpha(\tau) \Delta \vec{R}_\beta(\tau) \right\rangle}{6V\tau}, \quad (2)$$

where V is the total volume of the system, $\Delta \vec{R}_\alpha(\tau)$ is the total displacement vector of atoms of species α during time-step τ. Starting from this definition and assuming that the system is sufficiently dilute such that it can be divided into kinetically independent subspaces called cluster, we define cluster transport coefficients [41, 42, 56] . These coefficients are intrinsic equilibrium properties of each cluster and the total transport coefficients are obtained from the relation

$$L_{\alpha\beta} = \sum_c [c]^{ne} L_{\alpha\beta}^{eq}(c), \quad (3)$$

where $L_{\alpha\beta}^{eq}(c)$ is the transport coefficient of cluster c (units of $\left[\mathrm{m^2s^{-1}}\right]$) , and $[c]^{ne}$ is the concentration of cluster c per unit volume, not necessarily an equilibrium concentration. Thus, Eq. 3 defines out-of-equilibrium macroscopic transport coefficients, and expanding these coefficients into larger clusters enables going beyond the dilute limit. Cluster transport coefficients defined this way have the same units as diffusion coefficients. In order to have the same

units between cluster transport coefficients and transport coefficients, the former must be divided by the atomic volume, while concentrations in Eq. 3 become site concentrations.

KineCluE aims at computing these cluster transport coefficients using the self-consistent mean-field theory[50, 52] as a function of strain and temperature. Since a change in the chemical potentials of the system affects only the cluster concentrations in Eq. 3, KineCluE is a crucial step in developing a general and efficient framework to provide accurate atomic-based kinetic properties for higher-order models such as object-kinetic Monte Carlo [59–65], cluster dynamics [66–69] or phase field models [70–72].

2.2. *Self-consistent mean-field theory*

The goal of the self-consistent mean-field (SCMF) theory is to compute transport coefficients as a thermodynamic–i.e. equilibrium–average of atomic jumps. A chemical potential gradient driving the system out-of-equilibrium is assumed, and the resulting flux is computed using a thermodynamic average. Transport coefficients are then identified from Eq. 1. The method has been described in details elsewhere [41, 52], and here we outline the main steps to obtain a different formulation, more suitable to be coded efficiently.

It is assumed that the system can be mapped onto a rigid lattice containing a number of lattice sites, each being occupied by a single atom or defect. The microscopic master equation controls the evolution of a system represented by a configuration vector $\mathbf{n}$ whose components are the site occupation numbers, n_i^α ($n_i^\alpha = 1$ if species α occupies site i in configuration $\mathbf{n}$, and $n_i^\alpha = 0$ if not):

$$\frac{dP(\mathbf{n}, t)}{dt} = \sum_{\tilde{\mathbf{n}}} \left[W(\tilde{\mathbf{n}}, \mathbf{n}) P(\tilde{\mathbf{n}}, t) - W(\mathbf{n}, \tilde{\mathbf{n}}) P(\mathbf{n}, t) \right].$$

(4)

$P(\mathbf{n}, t)$ is the probability of having configuration $\mathbf{n}$ at time t, and $W(\tilde{\mathbf{n}}, \mathbf{n})$ is the rate at which a system in configuration $\tilde{\mathbf{n}}$ switches to configuration $\mathbf{n}$. It is assumed that the probability of any configuration can be expressed as the product of its equilibrium probability $P_0(\mathbf{n})$ and a probability $\delta P(\mathbf{n}, t)$

that corresponds to the deviation from equilibrium $P(\mathbf{n}, t) = P_0(\mathbf{n}) \times \delta P(\mathbf{n}, t)$, and that $\delta P(\mathbf{n}, t)$ has the same mathematical form as the equilibrium probability. However, thermodynamic interactions are replaced by an effective Hamiltonian in $\delta P(\mathbf{n}, t)$, to account for the fact that two equivalent configurations at equilibrium do not necessarily have the same probability in out-of-equilibrium conditions because the driving force breaks the symmetry of the system. In our formulation of the SCMF theory, the effective Hamiltonian is reduced to n_c-body effective interactions where n_c is the number of components (defects, solutes) in cluster c. The introduction of a driving force reduces the symmetry of the system such that only the crystal symmetry operations conserving the chemical potential gradient direction are valid for the out-of-equilibrium system. We group all symmetry-equivalent (in the out-of-equilibrium system) configurations into effective interaction classes because all of these configurations will equally contribute to the non-equilibrium averages. The magnitude of effective interactions belonging to class σ is denoted ν_σ and n_σ represents a product of site occupancies for each of the n_c cluster components, times a sign variable. Hence, for a given configuration, $n_\sigma = \pm 1$ if this configuration is identical to one of the instances of class σ, and $=0$ if it is not. Knowing the sign variable for one instance of the effective interaction class, the sign variable of another instance is the same if the symmetry operation that transforms one instance in the other maintains the chemical potential gradient vector, and the sign variable will be the opposite if the symmetry operation transforms the chemical potential vector into its opposite.

$$\delta P(\mathbf{n}, t) = \exp\left(\delta\Omega + \sum_{i,\alpha} n_i^\alpha \frac{\delta\mu_i^\alpha}{k_B T} - \sum_\sigma n_\sigma \frac{\nu_\sigma}{k_B T} \right).$$

(5)

$\delta\mu_i^\alpha$ is the local (site i) deviation from the equilibrium chemical potential of species α and $\delta\Omega$ is a normalizing constant. These quantities ($\delta\Omega, \delta\mu_i^\alpha, \nu_\sigma$) are time-dependent, but we are only interested in the steady-state flux, thus the time dependence is omitted for simplicity. Note that using only n_c-body effective interactions to describe the deviation from equilibrium

4

is not restrictive because it fully characterizes a system of n_c conserving defects and solutes in a bulk matrix.

The continuity equation per site reads:

$$\frac{d\,[\alpha]_i}{dt} = -\oiint_S \vec{J}_i^\alpha.d\vec{S} = -\sum_{s\epsilon\theta_i^\alpha}\Gamma_{i\to s}^\alpha, \qquad (6)$$

where $[\alpha]_i$ is the probability of site i to be occupied by species α (hence the local site concentration), J_i^α is the local flux per unit surface of species α from site i, and $\Gamma_{i\to s}^\alpha$ is the rate at which atoms of species α jump from site i to site s, the latter being located at jumping distance from site i ($s\epsilon\theta_i^\alpha$). The site concentration of species α on site i is also given by the first moment of the probability distribution function:

$$[\alpha]_i = \langle n_i^\alpha \rangle^{oe} = \sum_{\mathbf{n}} n_i^\alpha P(\mathbf{n},t). \qquad (7)$$

$\langle.\rangle^{oe}$ denotes the ensemble average over the out-of-equilibrium distribution function $P(\mathbf{n},t)$. We combine Eqs. 4-7 to obtain the atomic-scale description of the local concentration variation over time:

$$\frac{d\,\langle n_j^\beta \rangle^{oe}}{dt} = \left\langle \sum_{\tilde{\mathbf{n}}} n_j^\beta W(\mathbf{n},\tilde{\mathbf{n}})\,[\delta P(\tilde{\mathbf{n}}) - \delta P(\mathbf{n})] \right\rangle$$

$$= \left\langle \sum_{\tilde{\mathbf{n}}} n_j^\beta W(\mathbf{n},\tilde{\mathbf{n}})\left[\sum_{i,\alpha}(\tilde{n}_i^\alpha - n_i^\alpha)\frac{\delta\mu_i^\alpha}{k_BT} \right.\right.$$

$$\left.\left. - \sum_\sigma (\tilde{n}_\sigma - n_\sigma)\frac{\nu_\sigma}{k_BT} \right]\right\rangle. \qquad (8)$$

The first equality makes use of the detailed balance $W(\tilde{\mathbf{n}},\mathbf{n})P_0(\tilde{\mathbf{n}},t) = W(\mathbf{n},\tilde{\mathbf{n}})P_0(\mathbf{n},t)$, and $\langle.\rangle$ denotes the ensemble average over the equilibrium distribution function $P_0(\mathbf{n})$, implying an implicit sum over all configurations $\mathbf{n}$. The second equality results from a first order expansion of the exponential function in Eq. 5. The expression in Eq. 8 can be greatly simplified because: 1) for transitions between two configurations $\tilde{\mathbf{n}}$ and $\mathbf{n}$ where atom β at site j does not move, all the terms in the bracket will cancel out when $\tilde{\mathbf{n}}$ and $\mathbf{n}$ are inverted in the double sum over all configurations of the system (one sum is written explicitly, while the other is implicit in the $\langle.\rangle$ symbol). Thus the sum over $\tilde{\mathbf{n}}$ is restricted to configurations

where β is one jump away from site j, that is the ensemble of sites $s\epsilon\theta_j^\beta$. Note that additional constraints might exist to make a jump possible, for instance a substitutional atom needs a vacancy on the destination site. These constraints, expressed as a product of site occupation numbers, are denoted m_{js}^β, and the rate $\left[s^{-1}\right]$ of such jump is ω_{js}^β; 2) all sites in the system are occupied, either by a "bulk-like" species or by a solute or defect. Thus only chemical potential differences appear $\delta\bar{\mu}_i^\alpha = \delta\mu_i^\alpha - \delta\mu_i^{\text{bulk}}$, and the sum over species α is restricted to defects and solutes belonging to the cluster; 3) the driving force is assumed homogeneous in the system: $\delta\bar{\mu}_k^\alpha - \delta\bar{\mu}_i^\alpha = i\vec{k}.\vec{\nabla}\bar{\mu}_\alpha = d_{ik}^\mu\nabla\bar{\mu}_\alpha$, where k is the location of species α after the jump and d_{ik}^μ is the jump distance projected along unit vector $\vec{e}_\mu$ which is collinear to the chemical potential gradient direction (d_{ik}^μ may be positive or negative):

$$\left\langle \sum_{s\epsilon\theta_j^\beta} n_j^\beta m_{js}^\beta \omega_{js}^\beta \left[\sum_\alpha \sum_{i,k} n_i^\alpha \tilde{n}_k^\alpha d_{ik}^\mu \frac{\nabla\bar{\mu}_\alpha}{k_BT}\right.\right.$$

$$\left.\left. - \sum_\sigma (\tilde{n}_\sigma - n_\sigma)\frac{\nu_\sigma}{k_BT} \right]\right\rangle = -\sum_{s\epsilon\theta_j^\beta}\Gamma_{j\to s}^\beta. \qquad (9)$$

The flux from site j along a particular diffusion direction $\vec{e}_d$ (unit vector) is obtained by summing $\Gamma_{j\to s}^\beta$ over all forward jumps weighted by $d_{js}^d/V_{at} = \vec{js}.\vec{e}_d/V_{at}$, V_{at} being the volume per site. Ensemble θ_{j+}^β indicates that the summation runs over jumps with a positive d_{js}^d only. The macroscopic flux along $\vec{e}_d$ in a system of volume V is then obtained as an average over all sites in the system:

$$\mathbf{J}_{d,\beta} = \vec{J}_\beta.\vec{e}_d = \frac{1}{V}\sum_j n_j^\beta \sum_{s\epsilon\theta_{j+}^\beta} d_{js}^d \Gamma_{j\to s}^\beta. \qquad (10)$$

Flux $\Gamma_{j\to s}^\beta$ is identified from Eq. 9 for each specific jump, and for convenience, we use a matrix notation: $\mathbf{J}_d = -\frac{1}{V}\left(\mathbf{\Lambda}_d^0\boldsymbol{\mu} - \mathbf{\Lambda}_d\boldsymbol{\nu}\right)$, where $\boldsymbol{\mu}$ and $\boldsymbol{\nu}$ are vectors which do not depend on the diffusion direction but rather on the chemical potential gradient direction. $\boldsymbol{\mu}$ is a vector of length $N_{species}$ whose components are $\nabla\bar{\mu}_\alpha/k_BT$ ($N_{species}$ being the number of species); $\boldsymbol{\nu}$ is a vector of length N_{inter} whose components are the values of the effective interactions ν_σ/k_BT (N_{inter} being

the number of effective interactions); $\mathbf{J}_d$ is a vector of length $N_{species}$ whose components are $\mathbf{J}_{d,\beta}$, the fluxes of each species in diffusion direction $\vec{e}_d$; $\mathbf{\Lambda}_d^0$ is a matrix of size $N_{species} \times N_{species}$ representing the uncorrelated contribution to diffusion in direction $\vec{e}_d$, while the correlated contribution in the same direction is contained in $\mathbf{\Lambda}_d$, a matrix of size $N_{species} \times N_{inter}$. The components of these two matrices are given hereafter:

$$\mathbf{\Lambda}_{d,\beta\alpha}^0 = \sum_j \sum_{s\epsilon\theta_{j+}^\beta} d_{js}^d \left\langle n_j^\beta m_{js}^\beta \omega_{js}^\beta \sum_{i,k} n_i^\alpha \tilde{n}_k^\alpha d_{ik}^\mu \right\rangle, \quad (11)$$

$$\mathbf{\Lambda}_{d,\beta\sigma} = \sum_j \sum_{s\epsilon\theta_{j+}^\beta} d_{js}^d \left\langle n_j^\beta m_{js}^\beta \omega_{js}^\beta (n_\sigma - \tilde{n}_\sigma) \right\rangle. \quad (12)$$

Values for the effective interactions are obtained from the stationarity of the $n_c{}^{th}$-moment equations $d\left\langle n_{i_1}^{\alpha_1} n_{i_2}^{\alpha_2} .. n_{i_n}^{\alpha_n} \right\rangle /dt = d\left\langle n_{\sigma_0} \right\rangle /dt = 0$ for each configuration of the system corresponding to one instance σ_0 of some effective interaction class σ:

$$\left\langle n_{\sigma_0} \sum_{j,\alpha} n_j^\alpha \sum_{s\epsilon\theta_j^\alpha} m_{js}^\alpha \omega_{js}^\alpha d_{js}^\mu \nabla\bar{\mu}_\alpha \right\rangle$$
$$= \left\langle n_{\sigma_0} \sum_{j,\alpha} n_j^\alpha \sum_{s\epsilon\theta_j^\alpha} m_{js}^\alpha \omega_{js}^\alpha d_{js}^\mu \sum_\sigma (\tilde{n}_\sigma - n_\sigma) \nu_\sigma \right\rangle. \quad (13)$$

Note that the thermodynamic average $\langle . \rangle$ reduces to one configuration only for each effective interaction σ_0. Also, the sum over site j and species α appears because any component of the n_c-component cluster can potentially move and create non-zero contributions to both sides of the equation. Equation 13 is more conveniently written in matrix format: $\mathbf{M}\boldsymbol{\mu} = \mathbf{T}\boldsymbol{\nu}$ with:

$$\mathbf{M}_{\sigma_0\alpha} = \left\langle n_{\sigma_0} \sum_j n_j^\alpha \sum_{s\epsilon\theta_j^\alpha} m_{js}^\alpha \omega_{js}^\alpha d_{js}^\mu \right\rangle, \quad (14)$$

$$\mathbf{T}_{\sigma_0\sigma} = \left\langle n_{\sigma_0} \sum_{j,\alpha} n_j^\alpha \sum_{s\epsilon\theta_j^\alpha} m_{js}^\alpha \omega_{js}^\alpha d_{js}^\mu (\tilde{n}_\sigma - n_\sigma) \right\rangle. \quad (15)$$

Then solving for effective interactions consists in inverting matrix $\mathbf{T}$, and we obtain $\boldsymbol{\nu} = \mathbf{T}^{-1}\mathbf{M}\boldsymbol{\mu}$.

This solution is inserted in the expression for the flux: $\mathbf{J}_d = -\frac{1}{V}\left(\mathbf{\Lambda}_d^0\boldsymbol{\mu} - \mathbf{\Lambda}_d\boldsymbol{\nu}\right) = -\frac{1}{V}\left(\mathbf{\Lambda}_d^0 - \mathbf{\Lambda}_d\mathbf{T}^{-1}\mathbf{M}\right)\boldsymbol{\mu}$ from which we identify cluster transport coefficients in diffusion direction $\vec{e}_d$: $L_{d,\beta\alpha}^{eq}(c) = \frac{1}{V}\left(\mathbf{\Lambda}_d^0 - \mathbf{\Lambda}_d\mathbf{T}^{-1}\mathbf{M}\right)_{\beta\alpha}$. The next section shows that $\mathbf{M}$ is proportional to $\mathbf{\Lambda}_\mu^t$, which allows to save memory and computational effort.

2.3. Relationship between M and Λ

The expressions for $\mathbf{M}$ and $\mathbf{\Lambda}$ present interesting similarities (Eqs. 12 and 14), and we show that $\mathbf{M}$ can be directly obtained from $\mathbf{\Lambda}$, and that it does not require additional calculations. On one hand, the components of $\mathbf{M}$ are a sum over all possible jumps from a given configuration–corresponding to some effective interaction–of thermodynamically averaged jump frequencies. On the other hand, the components of $\mathbf{\Lambda}$ are a sum over all possible effective interactions for a given jump. We now derive the relation between coefficients $\mathbf{M}_{\sigma_0\alpha}$ and $\mathbf{\Lambda}_{\mu,\alpha\sigma}$, where α is an atom or defect species and σ represents an effective interaction class and σ_0 one particular instance of this class.

Taking a class of effective interactions σ, all of its instances give the same contribution to the $\mathbf{M}$ matrix (in absolute value, the sign might differ). Assuming that there are N_σ such instances per site we sum the $\mathbf{M}_{\sigma_0\alpha}$ components over the ones having a positive contribution, and the ones having a negative contribution:

$$N_\sigma \mathbf{M}_{\sigma_0\alpha} = \sum_{\sigma_0\epsilon\sigma_+} \mathbf{M}_{\sigma_0\alpha} - \sum_{\sigma_0\epsilon\sigma_-} \mathbf{M}_{\sigma_0\alpha}. \quad (16)$$

Also the projection of the jump distance along the chemical potential gradient direction can have a positive or negative contribution such that the sum over sites s in Eq. 14 is divided in two parts:

$$N_\sigma \mathbf{M}_{\sigma_0\alpha} = \sum_j \left(\sum_{\sigma_0\epsilon\sigma_+} \sum_{s\epsilon\theta_{j+}^\alpha} \chi \left| d_{js}^\mu \right| - \sum_{\sigma_0\epsilon\sigma_+} \sum_{s\epsilon\theta_{j-}^\alpha} \chi \left| d_{js}^\mu \right| \right.$$
$$\left. - \sum_{\sigma_0\epsilon\sigma_-} \sum_{s\epsilon\theta_{j+}^\alpha} \chi \left| d_{js}^\mu \right| + \sum_{\sigma_0\epsilon\sigma_-} \sum_{s\epsilon\theta_{j-}^\alpha} \chi \left| d_{js}^\mu \right| \right), \quad (17)$$

where $\chi = \left\langle |n_{\sigma_0}| \, n_j^\alpha m_{js}^\alpha \omega_{js}^\alpha \right\rangle$.

In Eq. 12, the flux has been computed in a given direction d. The absolute value of the reverse flux is identical, because of translational invariance. It follows that:

$$2\Lambda_{d,\alpha\sigma} = \sum_j \left(\sum_{s\epsilon\theta_{j+}^\alpha} |d_{js}^d| \left\langle (n_\sigma - \tilde{n}_\sigma) \, n_j^\alpha m_{js}^\alpha \omega_{js}^\alpha \right\rangle \right.$$
$$\left. - \sum_{s\epsilon\theta_{j-}^\alpha} |d_{js}^d| \left\langle (n_\sigma - \tilde{n}_\sigma) \, n_j^\alpha m_{js}^\alpha \omega_{js}^\alpha \right\rangle \right). \quad (18)$$

The final configuration of a given jump being the initial configuration of the reverse jump: $d_{js}^d \left\langle \tilde{n}_\sigma n_j^\alpha m_{js}^\alpha \omega_{js}^\alpha \right\rangle = -d_{sj}^d \left\langle n_\sigma n_s^\alpha m_{sj}^\alpha \omega_{sj}^\alpha \right\rangle$ and the minus sign comes from the fact that a given jump necessarily has a contribution to Λ which is opposite to that of the reverse jump. Using translational invariance:

$$\sum_j \sum_{s\epsilon\theta_{j+}^\alpha} d_{sj}^d \left\langle n_\sigma n_s^\alpha m_{sj}^\alpha \omega_{sj}^\alpha \right\rangle = \sum_j \sum_{s\epsilon\theta_{j-}^\alpha} d_{js}^d \left\langle n_\sigma n_j^\alpha m_{js}^\alpha \omega_{js}^\alpha \right\rangle. \quad (19)$$

Hence, Eq. 18 becomes:

$$2\Lambda_{d,\alpha\sigma} = \sum_j \left(2 \sum_{s\epsilon\theta_{j+}^\alpha} |d_{js}^d| \left\langle n_\sigma n_j^\alpha m_{js}^\alpha \omega_{js}^\alpha \right\rangle \right.$$
$$\left. - 2 \sum_{s\epsilon\theta_{j-}^\alpha} |d_{js}^d| \left\langle n_\sigma n_j^\alpha m_{js}^\alpha \omega_{js}^\alpha \right\rangle \right). \quad (20)$$

The last step is to explicit the sum over instances of the effective interaction class σ, which is hidden in the thermal average $\langle . \rangle$. As previously, this sum is separated into positive and negative contributions:

$$\Lambda_{d,\alpha\sigma} = \sum_j \left(\sum_{\sigma_0\epsilon\sigma_+} \sum_{s\epsilon\theta_{j+}^\alpha} \chi |d_{js}^d| - \sum_{\sigma_0\epsilon\sigma_+} \sum_{s\epsilon\theta_{j-}^\alpha} \chi |d_{js}^d| \right.$$
$$\left. - \sum_{\sigma_0\epsilon\sigma_-} \sum_{s\epsilon\theta_{j+}^\alpha} \chi |d_{js}^d| + \sum_{\sigma_0\epsilon\sigma_-} \sum_{s\epsilon\theta_{j-}^\alpha} \chi |d_{js}^d| \right). \quad (21)$$

Comparing Eqs. 17 and 21, $\Lambda_{d,\alpha\sigma}$ and $M_{\sigma_0\alpha}$ have the same structure. They differ by a factor N_σ which

is the number of instances in a given effective interaction class and by the direction along which the jump vector is projected d_{js}^d and d_{js}^μ, respectively. Taking the diffusion direction as the chemical potential gradient direction:

$$N_\sigma M_{\sigma_0\alpha} = \Lambda_{\mu,\alpha\sigma}, \quad (22)$$

and N_σ is easily obtained from symmetry operations for the out-of-equilibrium crystal. The components of the **M** matrix do not depend on the diffusion direction, but rather on the chemical potential gradient direction $\vec{e}_\mu$. Therefore, as long as $\vec{e}_\mu$ is taken as one of the diffusion directions (which is always the case in KineCluE) computing **M** can be avoided.

It is noteworthy that this relation (Eq. 22) guarantees that the cluster transport coefficient matrix is symmetric, at least for $d = \mu$. Let us define a diagonal matrix **N** which contains the N_σ coefficients. Then $\Lambda_\mu^t = \mathbf{NM}$ and the cluster transport coefficient matrix is expressed as:

$$\mathbf{L}_d^{eq}(c) = \frac{\Lambda_d^0 - \Lambda_d \mathbf{T}^{-1} \mathbf{N}^{-1} \Lambda_\mu^t}{V} = \frac{\Lambda_d^0 - \Lambda_d \tilde{\mathbf{T}}^{-1} \Lambda_\mu^t}{V}, \quad (23)$$

with $\tilde{\mathbf{T}} = \mathbf{NT}$. Because of detailed balance $\tilde{\mathbf{T}}$ is symmetric, thus $\mathbf{L}_\mu^{eq}(c)$ is also symmetric.

3. Software implementation

KineCluE is a set of Python scripts aimed at the computation of the transport coefficients of a cluster, typically consisting of point defects and/or impurities embedded in an infinite lattice. In this respect, it generalizes previous codes dedicated to the application of the SCMF method to specific diffusion mechanisms [38, 41, 73]. It is run in a Python 3.6 environment, with no need for high-performance computational facilities. It consists mainly of three files: a module containing the definitions of all classes and functions, and two scripts to perform the calculation, first in symbolic and then in numeric form. The former computes the flux equations (Eq. 9) and produces the list of configurations and jump frequencies that need to be considered within the specified interaction radius, whereas the latter performs the actual numerical calculation after the user has provided the relevant binding and saddle-point energies.

7

The code is highly versatile in terms of crystal structures, defects, cluster size, and jump mechanisms. It can treat diffusion of interstitial solutes, vacancies, dumbbells, as well as more complex, possibly multicomponent defects. Many point defect-mediated diffusion mechanisms for substitutional impurities can be modeled, from the traditional to the more complex ones, e.g., the recently theorized half-vacancy mechanism characterizing the diffusion of oversized solute atoms [55] (see Sec. 4.2.2) . It works for any crystal structure that can be described by some periodic vectors and a set of basis atoms, and in principle for clusters of any size and composition, although there are some practical limitations due to computational time increase with cluster size (see Sec. 4.1.1).

In addition to the tensor of transport coefficients in three user-defined diffusion directions, the code computes the cluster partition function as well as drag ratios, correlation factors, and other relevant cluster properties such as mobilities and dissociation probabilities, quantities that are required for higher scale models such as cluster dynamics and object kinetic Monte Carlo.

3.1. Overview

The logical diagram of the code is depicted in Fig. 1. We present here the main features relating the technical implementation to the SCMF theory exposed in the previous section. For more details and practical instructions, we refer the reader to the code documentation.

User input. The main ingredients for the symbolic calculation are the crystal periodicity vectors and basis atoms, the cluster components and their sublattices (also called "defects"), and the jump mechanisms. Each of these is represented in the code by an instance of the corresponding class (*Crystal*, *Defect*, *Species*, *JumpMech*). In addition, the SCMF method requires the definition of a kinetic radius, i.e. the cutoff distance for effective interactions. To a longer kinetic radius corresponds a higher amount of effective interactions, and hence a larger system of equations; this ensures a better accuracy because more kinetic trajectories are included. Optionally, a second (smaller) cutoff range can be set for thermodynamic interactions, with the aim of speeding up the
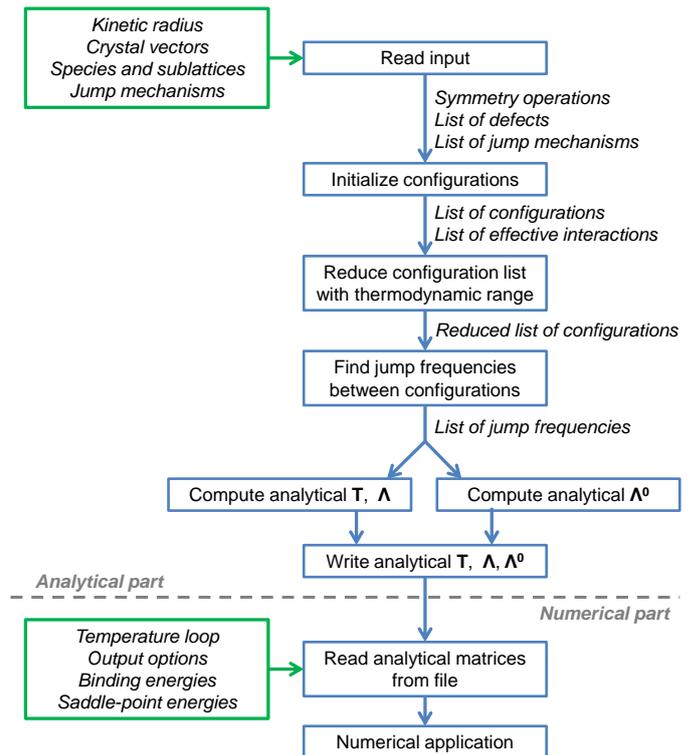

Figure 1: Overview of the main steps of the KineCluE code. Green boxes picture user inputs, and blue boxes represents some computation made by the code. The outputs of this computation are listed below each box. Note that the code consists of two parts: first the analytical calculation is performed; second the numerical application uses outputs from the analytical part to produce cluster transport coefficients.

calculations and reducing the amount of binding and saddle-point energies to compute. This is usually justified by the fact that binding energies between cluster constituents fade quickly with distance. The thermodynamic radius parameter should be set to the minimum value that allows for a correct description of thermodynamic interactions. The optimal choice of the kinetic radius parameter is discussed in Sec. 4.1.2.

Symmetry operations. KineCluE uses crystal symmetries to minimize the amount of effective interactions. At the beginning of the symbolic calculation, the symmetry operations conserving the crystal are computed using an algorithm inspired by the one from Trinkle[45], and then applied to find all symmetry-equivalent sublattice positions, cluster configurations, and jumps. In this way, the user needs to specify only sublattices and jump mechanisms that are unique with respect to all possible symmetry operations.

Interactions and jump frequencies. Symmetry operations are also employed to construct the phase space of cluster configurations (see Sec. 3.2) and classify the configurations in classes of symmetry-equivalent thermodynamic and effective interactions. For each newly found configuration, the symmetry operations are applied to each cluster component to produce all symmetric configurations, which are then assigned the same thermodynamic interaction. Analogously, effective interactions classes are identified by using the subset of symmetry operations that maintain the direction of the chemical potential gradient. In addition, symmetries are exploited to determine the list of symmetry-unique jump frequencies. For each allowed jump from an initial to a final configuration, the code applies the symmetry operations on the initial and final positions of the components *simultaneously*. This ensures that jumps with different saddle points but same initial or final positions are properly distinguished, as shown in [43, 74] for hexagonal close-packed structures. In the course of the development of KineCluE, the same subtlety was found also in Bravais lattices, as is shown in Fig. 2. This demonstrates the need for using crystal symmetry analysis to identify unique transitions.
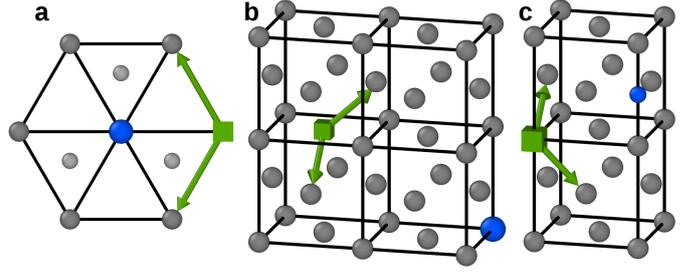

Figure 2: Examples of vacancy (green square) jumps in the vicinity of a solute (blue sphere) for various lattices: a) hexagonal close pack, the smaller and lighter spheres representing atoms that are below and above the basal plane; b) face-centered cubic with a substitutional solute; c) face-centered cubic with an interstitial solute. For each system, the two jumps shown with green arrows are not equivalent because of differing saddle-point configurations, even though the initial and final configurations are symmetrically identical.

Symbolic computation. Once the lists of interactions and jump frequencies are finalized, the code proceeds to the symbolic calculation of $\mathbf{T}$ (Eq. 15), $\mathbf{\Lambda}$ (Eq. 12), and $\mathbf{\Lambda}^0$ (Eq. 11) ($\mathbf{M}$ is directly obtained from $\mathbf{\Lambda}$, as explained in Sec. 2.3). The $\mathbf{T}$ matrix is built line by line by looping on the list of symmetry-unique effective interactions: for each configuration containing this effective interaction, the code explores all configurations that can be reached with a valid jump, recognizes the effective interaction corresponding to each final configuration, and assigns the transition to the corresponding jump frequencies ω_{ij}. The initial configuration brings in a negative contribution ($-\omega_{ij}$), and the final configuration a positive one ($+\omega_{ij}$) to the matching column of the $\mathbf{T}$ matrix. In the case of homogeneous driving forces, kinetic correlations only depend on the anti-symmetric part of the effective interactions [51]. Hence, the contribution is swapped in sign if the symmetry operation leading to this particular instance of the effective interaction class reverses the chemical potential gradient direction. Concurrently, each column of the $\mathbf{\Lambda}$ matrix is obtained by averaging each species displacement (projected on the chemical potential gradient direction) among all valid jumps from each effective interaction configuration. The uncorrelated term $\mathbf{\Lambda}^0$ is instead obtained by averaging each species net displacement (with no projections) over all possible thermodynamic states of the system. Finally, the code computes the parti-

tion function $Z = \sum_t g_t \exp\left(E_b^t/k_B T\right)$, where t marks the thermodynamic interaction, E_b^t the binding energy (positive means attraction) and g_t the geometric multiplicity, i.e. the number of symmetry equivalents (which fully accounts for configurational entropy inside the cluster). At this point, the symbolic calculation is done and the results are stored in a file to be loaded back by the numerical part of the code.

Strained systems. The symmetry-based approach allows for a straight-forward treatment of strained systems. The user can define a strain tensor to deform the crystal and reduce its symmetry. The code automatically finds the subset of symmetry operations that remain valid, and evaluates if the broken symmetry gives rise to new symmetry-unique sublattices or jump mechanisms that were equivalent in the unstrained system, updating the list of effective interactions and jump frequencies accordingly. The calculation of the symbolic expressions then proceeds in the same way. Strains usually generate anisotropic diffusion terms [53], which appear in the code as non-null terms along the directions perpendicular to the chemical potential gradient direction. Note that we introduce single component effective interactions to account for kinetic correlations of a single defect in a non-Bravais strained lattice.

Numerical evaluation. For the numerical calculations, the user provides a range of temperatures and (optionally) strain values, as well as the binding and saddle point energies for each of the symmetry-unique configurations and jump frequencies found in the symbolic part of the code. The latter are listed in separate files, so that they can be inspected in an atomic visualization software, and computed with the usual methods (density functional theory, interaction models, interatomic potentials, *etc.*). For strain calculations, the user needs to provide as well values of the elastic dipoles of each equilibrium and saddle-point configuration; the energy variation due to elastic energy is computed automatically within the linear elasticity theory [75]. The calculation at this point simply consists in solving numerically the system of equations of Eq. 13, and combining the results with matrices $\mathbf{\Lambda}$ and $\mathbf{\Lambda}^0$ as in Eq. 23. Additional options allow the user to perform parametric

studies as functions, for instance, of the kinetic radius (see Sec. 4.1.2), of particular jump frequencies, as well as sensitivity studies to identify the jump frequencies that have the largest impact on the cluster transport coefficients (see Sec. 4.1.3).

After computing the coefficients for each cluster (one calculation each), the total transport coefficients in Eq. 3 must be computed as a post-processing step, depending on the cluster concentrations [c] that can be obtained either in equilibrium or non-equilibrium conditions, for instance by linking with a cluster-dynamics model.

Computational load. From a computational perspective, the code is light and can easily run on personal laptops. Distributed under an LGPL license, it can be downloaded freely together with the user documentation and a set of input file examples[76]. The computational time can be as short as one second for two-component clusters, and increases with cluster size, kinetic radius, and the amount of jump mechanisms. Increasing the kinetic radius or the number of components involves in both cases a wider configuration space and a higher amount of kinetic equations, the construction of which is the bottleneck of the symbolic calculation. See Sec. 4.1.1 for a more detailed evaluation of the computational time with cluster size and kinetic radius.

Current limitations. Among the limitations of the current version of KineCluE, the most important to mention is that it proceeds in the canonical ensemble (fixed number of atoms of each species) and with a fixed number of defects and solutes. The first condition implies that users keep track of the number of matrix atoms involved in their system, even though they are not declared explicitly. One example is an interstitial solute becoming a substitutional solute where an implicit matrix atom was located. As in a Monte Carlo simulation in the canonical ensemble, this matrix atom cannot disappear, and must become for instance a self-interstitial atom. Users must also pay attention to the second condition. For instance, recombinations between self-interstitials and vacancies cannot be modeled at this stage, because such a reaction would lead from a two-component cluster (the two point defects) to no defects. This limitation can sometimes be overcome by allowing two defects

to be located at the same site (cf. the code documentation, and the kick-out mechanism described in Sec. 4.2.3). Finally, no transmutations (change of defect type or solute species) are allowed in the definition of the jump mechanisms.

3.2. *Configuration space exploration algorithm*

We present in more details our–to the best of our knowledge–original algorithm to explore and build the cluster configuration space. Such an algorithm can be useful outside the scopes of KineCluE, for instance to sample the configuration space and perform exact thermodynamic averages, in replacement of traditional rigid-lattice Monte Carlo simulations. From a starting configuration (that can be either provided by the user or automatically generated) the algorithm applies the user-defined jump mechanisms to move from one configuration to the next one. In this sense, the configuration space can be seen as a graph where the nodes (the configurations) are connected with each other by a jump. Symmetry operations are used at each newly found configuration to ensure that symmetry-equivalent configurations are visited only once.

Figure 3 summarizes the main steps of the algorithm. Configurations to analyze are progressively appended to an exploration list, which initially includes the starting configuration only, and all found configurations are stored in the final configuration list. The exploration stops when the exploration list is empty. For each new configuration C in the exploration list, the code first generates all symmetry-equivalent configurations and appends them to the configuration list, then considers all jumps applicable from C. Each final configuration reached by the latter jumps is added to the exploration list, unless it is found to be disconnected, i.e. if any component of the cluster is found at a distance larger than the defined kinetic radius from any other cluster component. Therefore, if the starting configuration is the most compact one, the algorithm builds the configuration space by moving progressively to configurations where the cluster constituents are further and further apart, until one or more of them are beyond the kinetic radius. However, the starting configuration does not need to be the most compact one: if defects, species permissions, and jump mecha-
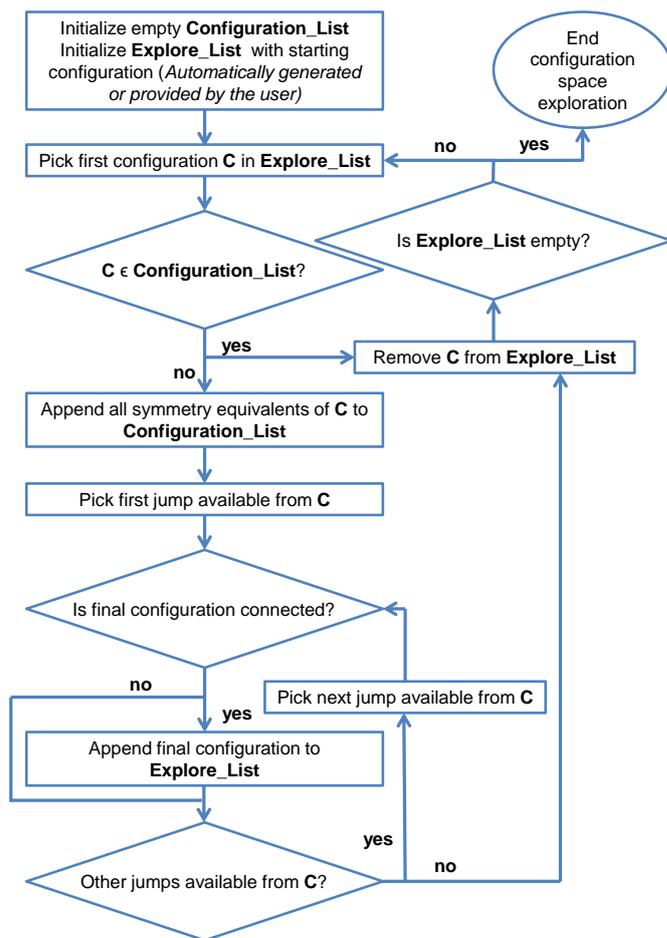

Figure 3: Algorithm for the exploration of the configuration space, using symmetry operations to minimize the number of configurations to explore.

nisms have been well defined, the resulting config-
uration space should be well connected and indepen-
dent from the chosen initial configuration. This is
also ensured by the fact that reverse jumps are added
automatically by the code if they are not found by
symmetry operations.

Finally, it should be noticed that a correct defini-
tion of the jump mechanisms is crucial for the al-
gorithm to visit all configurations existing within the
defined kinetic radius, and that not necessarily all the
connected configurations are reachable with a given
set of jumps. For instance, in the case of a dumbbell-
solute pair with radius equal to the 1NN distance,
the so-called tensile configurations (solute in a non-
target 1NN position) are not accessible, unless an on-
site rotation jump is defined [37].

4. Testing and applications

In this section we assess the technical performance
and current limitations of the code, discuss the con-
vergence of transport coefficients with respect to the
kinetic radius, and explain how to perform sensitivity
studies to identify the most important jump frequen-
cies of the system.

4.1. Performance and functionality assessment

4.1.1. Assessment of computation time and memory

In the analytical part of the code, most of the
time is spent on the construction of the configura-
tion space and of the analytical system of equations.
Therefore, the parameters most affecting the compu-
tational performance are the kinetic radius and the
cluster size, because they are both proportional to
the amount of configurations and of kinetic inter-
actions. Figure 4 shows measurements of the com-
putational time as functions of these two quanti-
ties, in the following sample cases: vacancy-solute
and dumbbell-solute pairs (kinetic radius, left panel);
clusters of vacancies and substitutional or intersti-
tial solutes (cluster size, right panel). The tests were
run on a workstation equipped with an Intel® Xeon®
CPU E5-2680 v4 processor (2.40 GHz). The timing
of the numerical code was averaged on the amount
of temperature-strain data points.

For both parameters, the computation time in-
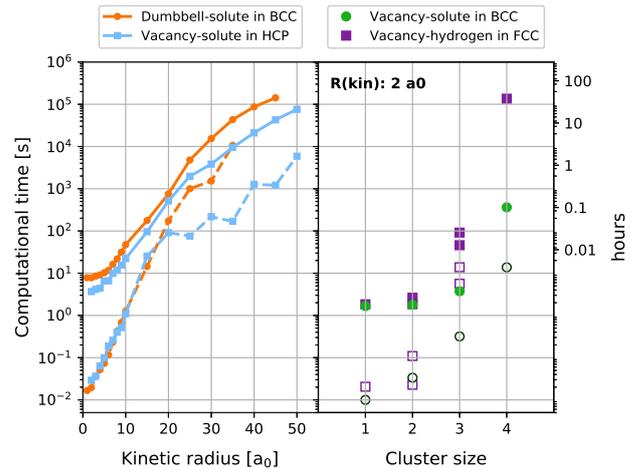creases quickly on the logarithmic scale. For what

Figure 4: Measured computational times as functions of kinetic
radius (left) and cluster size (right) on an Intel® Xeon® CPU
E5-2680 v4 (2.40 GHz). The measurements of numerical cal-
culations, marked with dashed lines and empty markers, refer
to the average time per computed temperature data point.

concerns the kinetic radius, this is of no issue be-
cause results are usually already well converged af-
ter a few lattice parameters, as is showed in the next
section. It is thus unneeded to go to very large radii,
and in the vast majority of cases it is possible to run
calculations in a matter of seconds or minutes, in any
case no longer than an hour.

On the contrary, computation time represents at
the moment a technical limitation for the cluster size
that can be handled in KineCluE. It will be necessary,
in order to extend its capabilities to larger clusters, to
implement parallelization strategies on the construc-
tion of the system of equations and of the configura-
tion space. Furthermore, another limitation is given
by memory requirements: in Figure 4, the tests could
not be performed beyond 45-50 a_0 and 4-5 compo-
nents because the RAM memory of the workstation
was completely filled up. The main limiting factors
also in this case are the amount of configurations
and effective interactions: for instance, a computa-
tion with 1.08 million configurations and 136 thou-
sands interactions required about 2.4 GB of RAM.
This issue will be addressed in future versions of the
code.

In conclusion, the current version of KineCluE is
limited to clusters of size 4 or 5, depending on the
chosen kinetic radius, whereas for pairs it is possible

to obtain very well converged results in reasonably short times on standard personal workstations.

4.1.2. Convergence of pair transport coefficients

The larger the kinetic radius, the more kinetic trajectories are included in the calculation. At infinite kinetic radius, all possible trajectories are included so the formalism adopted in KineCluE should theoretically converge towards the exact value for an isolated cluster in an infinite medium. This paragraph shows that cluster transport coefficients converged within practical errors are obtained for kinetic radii no larger than a few lattice parameters. The investigation is summarized in Fig. 5, and was performed for various crystallographic systems, jump mechanisms and temperatures, each informed by previously published *ab initio* calculations[43, 55, 73, 77], so convergence varies from one system to another.

In a dilute system containing only monomers and pairs, all the off-diagonal contributions to the Onsager matrix come from interactions within the defect-solute (dS) pair cluster. Hence, we know that the product between the off-diagonal cluster transport coefficient $L_{dS}(dS)$ and the pair partition function Z_{dS} converges towards a well-defined physical quantity. Therefore, we choose the absolute value of the relative error on the $Z_{dS} \times L_{dS}(dS)$ product, to evaluate convergence and to choose the most appropriate kinetic radius, which should: 1) be sufficiently high so that all important kinetic trajectories are taken into account (converged quantity); 2) be sufficiently low so that all cluster in the solid solution remain isolated from each other (dilute hypothesis, see Sec. 2.1). Once the kinetic radius is set for the pair cluster, it should be kept identical for all clusters in the system, otherwise illogical configurations would arise, for instance a three-body configuration where all components interact as pair clusters but the configuration is not considered as a three-body cluster (or the opposite).

Figure 5 shows the absolute value of the relative error on $Z_{dS} \times L_{dS}(dS)$ with respect to its value at $R_{kin} = 20$ a_0 taken as reference. First of all, this contribution is indeed converging monotonically with increasing kinetic radius. Second, the sign of the relative error (shown as solid and dashed lines) varies from one example to another, but it is correlated with
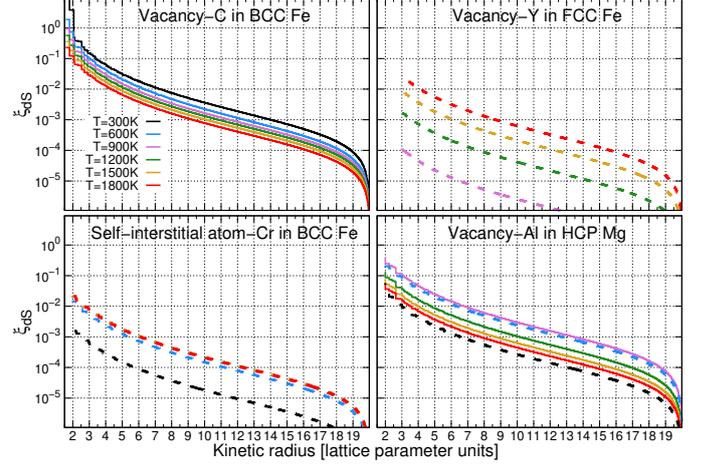

Figure 5: Convergence of cluster transport coefficients as a function of the kinetic radius for various crystallographic systems and jump mechanisms. ξ_{dS} is the absolute value of the relative error on the $Z_{dS} \times L_{dS}(dS)$ product, the reference value being taken at a kinetic radius of 20 lattice parameters. Solid (resp. dashed) lines represent positive (resp. negative) values of the relative error. Note that in the bottom-left plot, all curves from $T = 900$ K upwards are superimposed.

the actual sign of off-diagonal transport coefficients. In the end, choosing a lower kinetic radius always leads to underestimated values of the absolute value of off-diagonal transport coefficients, which is logical since this coefficient mainly contains contributions from correlated trajectories. The larger the kinetic radius, the more of these correlated trajectories are added to the calculation, even though their thermodynamic weight decreases with increasing distance. This is consistent with findings from variational approaches of transport coefficients [48, 49]. Another interesting point is the evolution of convergence with temperature. We found that increasing the temperature always leads to a decrease in the value of off-diagonal transport coefficients, such that the relative error increases if these coefficients are positive, while it decreases if they are negative. This behavior is observed in Fig. 5 by looking at the order of the curves depending on whether they are solid or dashed. Finally it is noteworthy that all relative errors drop below 10% at a kinetic range of three lattice parameters. Although this may not be true for other examples, the variety of jump mechanisms and interactions strongly points towards the validity and applicability of our cluster transport coefficients formalism to a wide variety of systems.

4.1.3. Sensitivity study

In this section we demonstrate how to use the sensitivity study routine of KineCluE, and how it can be useful in parameterizing the kinetic model efficiently. As an example, we consider the diffusion of a vacancy-carbon pair (*VC*) in Fe, and rely on previously published *ab initio* data[77]. After the analytical part of the code, a set of jump frequencies are identified, and the user needs to supply numerical values for the saddle-point energies corresponding to all of these jump frequencies. If saddle-point energies are not provided, KineCluE will use by default the kinetically-resolved activation (KRA) barrier approximation[78] based on the binding energies of the initial and final state (in our example we assume that all binding energies have been computed accurately):

$$E_{\mathrm{sp}}^{\alpha} = Q^{\alpha} - \frac{E_{\mathrm{b}}^{\mathrm{ini}} + E_{\mathrm{b}}^{\mathrm{fin}}}{2}, \qquad (24)$$

where E_{sp}^{α} is the saddle-point energy for a jump performed by species α between two configurations which are characterized by binding energies $E_{\mathrm{b}}^{\mathrm{ini}}$ and $E_{\mathrm{b}}^{\mathrm{fin}}$ (positive binding energy means attraction). Q^{α} is a species-specific activation energy, usually taken as the bulk migration energy of this species when it is isolated.

Unfortunately, we cannot tell beforehand how well this approximation performs for a given jump, and a change in saddle-point energies may lead to qualitative changes in transport coefficients. Still, we use the default (i.e. KRA) value of saddle point energies as a starting point for the sensitivity analysis. The theory behind this analysis is described in details in the Appendix section. It is an iterative process, and each row of Fig. 6 corresponds to one step of the process. Each step itself consists of two parts. The first part is the computation of the gradient of cluster transport coefficients in the jump frequency space, which is simply the partial derivative of cluster transport coefficient with respect to each jump frequency. The larger the partial derivative, the larger the change in transport coefficients resulting from a change in the saddle-point energy of the corresponding jump frequency. Note that dissociation jump frequencies should be removed from this analysis. Indeed, numerous jump frequencies can be assigned to a disso-

ciation frequency, *e.g.* all jumps between the thermodynamic and kinetic radius. This way, dissociation jump frequencies are made artificially important because of how we regroup jump frequencies together to speed up the calculation. Moreover, they should in principles represent jumps where cluster components do not interact anymore, such that the KRA approximation in Eq. 24 is expected to hold. The second part is to compute the values of cluster transport coefficients for different values of the most critical jump frequencies, which helps in deciding if it is worth computing these jump frequencies accurately, for instance using *ab initio* methods.

The left-hand side column of Fig. 6 shows the normalized gradient at each step, and allows to identify the most important jump frequencies. Obviously, some jump frequencies affect a lot some coefficients of the Onsager matrix and do not have much effect on other coefficients. To simplify the discussion in this example, we focus on the off-diagonal coefficient at $T = 600$ K. The first step of the calculation identifies jump frequencies C_{56} and C_{12} as having the most effect on the L_{VC} coefficient. The right-hand side column of Fig. 6 shows the ratio between the L_{VC} coefficient for various values of these two jump frequencies and the current L_{VC} value. We see that variations of 0.2 eV in saddle-point energies can produce a change in the qualitative nature (i.e., sign) of flux coupling between vacancy and carbon. It is thus important to have an accurate estimation of these jump frequencies. In Ref. [77]–using *ab initio* calculations–the saddle-point energies are found respectively -0.055 eV and -0.445 eV higher than the KRA-predicted value, which results in a change of sign of the L_{VC} coefficient as well as a one order of magnitude increase in its absolute value. Going to the second iteration of the process, jump frequencies C_{56} and C_{12} are set to their *ab initio* values and thus removed from the analysis. Jump frequencies V_{25} and V_{12} are now identified as the most critical ones. Again, the right-hand side plot shows that a small variation of the V_{12} jump frequency value could lead to a change of sign of L_{VC}, so this jump frequency needs to be calculated accurately. On the contrary, jump frequency V_{25} does not seem to have much effect on L_{VC} unless the saddle-point energy is found about 0.3 eV lower than the current KRA value. In

fact, *ab initio* calculations show that the V_{12} jump is not possible (which leads to a change of sign of L_{VC}), and that the V_{25} saddle-point energies is only 0.05 eV higher than the KRA-predicted value. Moving on to the third step and removing jump frequencies V_{25} and V_{12} from the analysis, jump frequencies C_{25} and C_{68} are identified as the most critical ones. But when we look at the right-hand side plot, we see that the impact of these two jump frequencies is rather small, unless the KRA approximation is off by about 0.5 eV for both jump frequencies, which is unlikely. Hence we can consider that we have already computed all the most important jump frequencies, and that the parameterization step can be stopped here.

On this simple example where the code identified 12 jump frequencies, the sensitivity analysis shows that one only needs to compute 4 of these jump frequencies to get a reasonable estimation of the L_{VC} coefficient. The value obtained after step 2 ($L_{VC} = -2.263 \times 10^{-14} \ m^2 s^{-1}$) is found to be within a 5% relative error with respect to the coefficient obtained when all 12 jump frequencies were computed *ab initio* ($L_{VC} = -2.388 \times 10^{-14} \ m^2 s^{-1}$). In larger clusters were hundreds of jump frequencies are identified by the code, this sensitivity analysis can result in important computational savings for the parameterization of the model while having accurate cluster transport coefficient values.

4.2. Benchmarking to literature studies

We briefly present in this section a few validation studies in a broad range of crystal lattices and diffusion mechanisms, including strained systems.

4.2.1. Self-diffusion correlation factors in various systems

A first validation consists in computing the self-diffusion correlation factors f_0 for several diffusion mechanisms. This is easily done in KineCluE by defining the tracer atom as a foreign species having the same exact energetics as the matrix host atoms. The latter entails null interaction energies, and jump frequencies equal to those in the pure metal.

Before anything else, let us define correlation factors: to us, a correlation factor is the ratio between a transport coefficient and the uncorrelated part of that same coefficient, meaning that coefficient reduced to
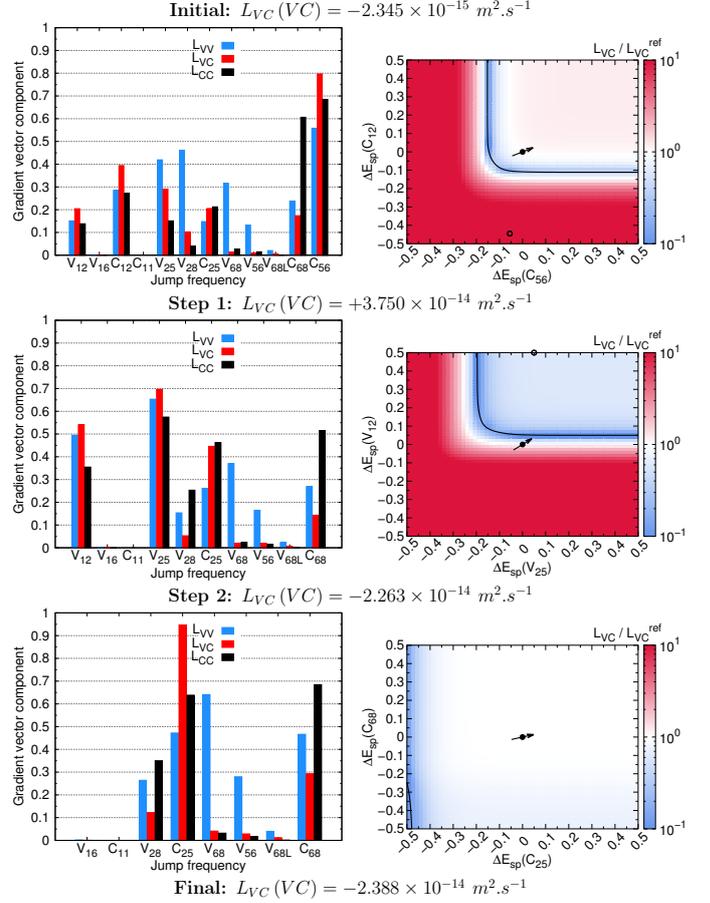

Figure 6: Example of sensitivity analysis using *ab initio* data[77] for a vacancy (*V*)–carbon (C) pair in Fe at $T = 600$ K. Each row corresponds to a step of the sensitivity study, the left-hand plot being the analysis of the most critical jump frequencies (i.e. the ones with the highest components in the normalized gradient vector), and the right-hand plot being the computation of transport coefficients for various saddle-point energy values for the two most critical jump frequencies. In the latter, the axes show saddle-point energy differences with respect to the KRA-computed value, while the color surface shows the absolute value of the ratio between the corresponding L_{VC} and its reference value before this step of the sensitivity study. The black contour indicates a change in the sign of L_{VC}. The filled circled represents the saddle-point energy values at which the reference L_{VC} was computed (0,0) and the arrow points towards the direction of highest variation of L_{VC}. Finally, the open circle shows the value of saddle-point energies differences once they were computed *ab initio* [77]. Jump frequencies are labeled α_{ij} for a jump where species α jumps between a configuration where *V* and C are i^{th} nearest-neighbors and a configuration where they are j^{th} nearest-neighbors.

its $\mathbf{\Lambda}_d^0$ component in Eq. 23. The uncorrelated part of a transport coefficient is a sum over all possible configurations and possible jumps from these configurations of the associated jump frequencies weighted by square jump distances. Most of the time, this definition of the uncorrelated contribution amounts to the definition given by a random walk. Yet, when defects go through different non-equivalent configurations, users needs to define macro-jumps between equivalent configurations to be able to compute a true random walk [79]. The arbitrary choice of macro-jumps may lead to different f_0 values because the sum only runs over a restricted number of configurations. For instance, considering dumbbell migration in FCC metals, f_0 is found equal to 0.439454 [80] or 0.878908 [79] depending on whether the random walk is defined between jumps or macro-jumps consisting of two successive jumps. Our definition based on $\mathbf{\Lambda}_d^0$ does not require any definition of macro-jumps, which makes it more general and systematic. Note that this definition only affects the f_0 coefficient, not transport coefficients.

Table 1 shows the computed f_0 in comparison with previous analytical or Monte Carlo calculations [15, 36, 55, 79–85], and when available with the Green function (GF) method by Trinkle [45]. As opposed to the latter, the results in KineCluE depend on the chosen kinetic radius R_{kin}, i.e., on the amount of kinetic trajectories included in the calculation. However, with increasing R_{kin} the results converge well to the reference values, and it is not necessary to go to very large radii to obtain an already satisfactory precision. For instance, a calculation with $R_{kin} = 6a_0$ runs in a few seconds and ensures a precision to the third or fourth decimal digit, which is usually fully satisfactory for the purposes of a diffusion study. It is interesting to mention that, in agreement with the convergence analysis in Section 4.1.2, the value of f_0 systematically decreases with increasing kinetic radius, as the contribution of correlations becomes larger.

We have investigated vacancy-exchange mechanisms in several crystals, including two-dimensional ones, and some dumbbell mechanisms in BCC and FCC alloys. The case of dumbbell–solute pairs in BCC has been more extensively treated in another work [73], where KineCluE has allowed for the extension of the previous SCMF framework [37] from first nearest-neighbor (1nn) interactions to arbitrarily long kinetic radii. The correlation factor obtained for the rotation-translation mechanism of ⟨100⟩ dumbbells in FCC is in full agreement with Monte Carlo simulations [87] and Bocquet's earlier analytical model [80].

In addition, we have successfully tested the code on a few more complex mechanisms, for which analytical calculations are available, namely: tracer diffusion in FCC via a di-vacancy mechanism [15], the diffusion of oversized atoms in BCC and FCC alloys [55], and several kick-out and combined dumbbell-direct interstitial mechanisms in diamond [83]. The latter two cases are discussed in more detail in Sections 4.2.2) and 4.2.3, respectively.

4.2.2. Oversized solute mechanism in BCC and FCC crystals

Thanks to the high degree of flexibility in the jump mechanism definition, KineCluE can handle complex diffusion mechanisms, such as for instance the recently discovered diffusion pattern of oversized solute atoms (OSA) in BCC and FCC alloys [55]. According to this mechanism, OSA diffusion does not occur via a direct exchange with vacancies; instead, when neighboring a vacancy, the oversized atom leaves the substitutional position and relaxes towards the center of the empty lattice space, forming a complex with two half vacancies. In this "split-vacancy" configuration, either of the two half vacancies can exchange with one of the neighboring matrix atoms. This entails the dissociation of the complex and the return of the solute into a substitutional position (Fig. 1 of the previous work [55]). A net displacement of the solute has occurred if the new substitutional position is different from the one before the complex formation. In FCC structures, it is also possible for the half-vacancy to perform non-dissociative jumps within the 1nn triangle (Fig. 3 of the previous work[55]). Bocquet and coworkers developed the analytical framework to compute the solute correlation factor and diffusion coefficient for this new mechanism, and then considered the case of yttrium in BCC and FCC iron by computing the *ab initio* migration barriers, with solute-vacancy thermodynamic interactions limited to 1nn and 2nn.

Table 1: Self-diffusion correlation factors for various mechanisms, as computed with KineCluE, in comparison with the Green function method [45] and previous calculations [15, 36, 55, 80–85]. The third column refers to the absolute error with respect to the reference value in the last column (or the GF method when available), when the calculation is performed with a smaller kinetic radius (6 a_0).

| Mechanism	KineCluE (R_{kin})		Error at $R_{kin} = 6a_0$	GF method[45]	other calculations
Vacancy mechanisms					
BCC	0.72719507	(50 a_0)	$4.8 \cdot 10^{-4}$	0.72719414	0.727194 [81, 85]
FCC	0.78145371	(30 a_0)	$2.7 \cdot 10^{-4}$	0.78145142	0.78145142 [81, 85]
Simple cubic	0.65310983	(60 a_0)	$8.5 \cdot 10^{-4}$	0.65310884	0.653109 [85]
HCP base plane	0.78121130	(30 a_0)	$7.2 \cdot 10^{-4}$	0.78120488	0.78120489 [84]
HCP axial plane	0.78145784	(30 a_0)	$7.2 \cdot 10^{-4}$	0.78145142	0.78145142 [84]
Diamond	0.50000082	(30 a_0)	$9.8 \cdot 10^{-5}$	0.50000000	0.5 [81, 84]
Dumbbell mechanisms					
$\langle 110 \rangle$ in BCC, 60°rotation-translation	0.41264390	(30 a_0)	$3.1 \cdot 10^{-4}$	-	0.413010 [36]
$\langle 110 \rangle$ in BCC, translation	0.49432350	(50 a_0)	$1.2 \cdot 10^{-3}$	-	0.494371 [36]
$\langle 100 \rangle$ in FCC, 90°rotation-translation	0.43945498	(30 a_0)	$1.0 \cdot 10^{-4}$	-	0.439454 [80]
Other mechanisms					
Divacancy mechanism in FCC	0.45809698	(30 a_0)	$3.0 \cdot 10^{-4}$	-	0.45809434 [15]
Oversized solute diffusion in BCC	0.76161942	(30 a_0)	$1.8 \cdot 10^{-3}$	-	0.761603 [55]
Oversized solute diffusion in FCC	0.79459770	(30 a_0)	$8.7 \cdot 10^{-3}$	-	0.787081 [55]
Kick-out mechanism in diamond					
Tetrahedral (t_{1-3})	0.9696972	(20 a_0)	$8.3 \cdot 10^{-6}$	-	0.969733 [86], 0.9701 [83]
Hexagonal ($h_{1,2}$)	0.851764	(20 a_0)	$2.4 \cdot 10^{-5}$	-	0.8525 [83]
Hexagonal ($h_{3,4}$)	0.917991	(30 a_0)	$3.5 \cdot 10^{-3}$	-	0.9269 [83]
Hexagonal (h_{5-8})	0.9925246	(20 a_0)	$4.0 \cdot 10^{-7}$	-	0.9927 [83]
Multiple interstitial mechanism in diamond					
Tetrahedral	0.4848494	(10 a_0)	$7.2 \cdot 10^{-6}$	-	0.4850 [83]
Hexagonal	0.5641879	(10 a_0)	$1.4 \cdot 10^{-3}$	-	0.5643 [83]
Vacancy in two-dimensional lattices					
Square lattice	0.46697619	(100 a_0)	$8.5 \cdot 10^{-3}$	-	0.46705 [82]
Hexagonal lattice	0.56009029	(100 a_0)	$8.5 \cdot 10^{-3}$	-	0.56006 [82]
Honeycomb structure	0.33336978	(100 a_0)	$9.5 \cdot 10^{-3}$	-	0.33333 [82]
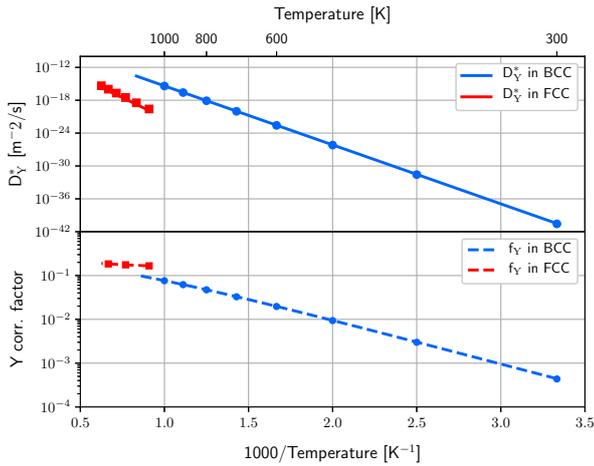
Figure 7: Diffusion coefficient (above) and correlation factor (below) of yttrium in BCC and FCC iron via the oversized solute diffusion mechanism, compared with the analytical calculations (markers) by Bocquet *et al.*[55].
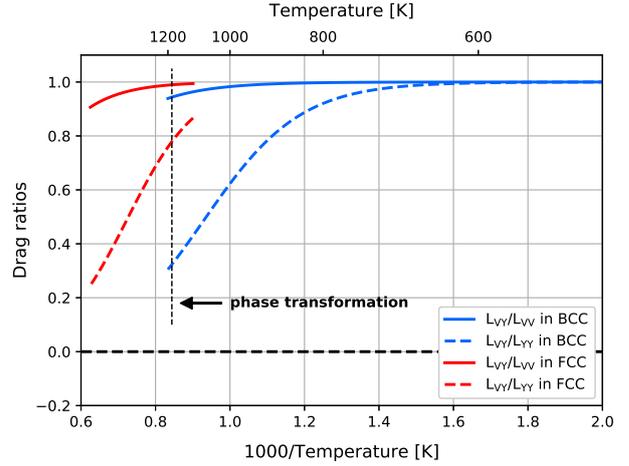

Figure 8: Variation with temperature of the off-diagonal to diagonal transport coefficient ratios, for diffusion of yttrium in BCC and FCC iron via the oversized solute mechanism.

With the appropriate definition of configurations and jumps, it is possible to reproduce the same mechanism in KineCluE. The split-vacancy configuration is defined by introducing a second sublattice in the intermediate position between two substitutional atoms, and by setting permissions so that each species (vacancy and solute) is allowed on that sublattice only when sharing the site with the other species. In addition, the usual 1nn substitutional configuration must be forbidden by setting its prefactor to zero in the numerical part of the code. Finally, the solute jump needs to be described with several dissociative jumps, each of which departs from the split-vacancy configuration and brings the vacancy either to a 2nn, 3nn, or 5nn configuration in BCC (2nn, 3nn, or 4nn in FCC). In FCC, it is also necessary to add the 1nn-1nn non-dissociative jump. Sample input files can be found in the code documentation. Figure 7 shows the perfect match between the Y correlation factor and diffusion coefficient obtained with KineCluE and Bocquet's analytical model. A satisfactory agreement is also obtained for the self-diffusion correlation factors shown in Table 1.

In addition, KineCluE provides a more complete picture of solute-defect correlations thanks to the calculation of the off-diagonal transport coefficient for kinetic radii larger than a few nearest neighbors. We have therefore computed the drag ratios L_{YV}/L_{YY} and L_{YV}/L_{VV} (Fig. 8) with Bocquet's *ab initio* migration barriers, setting the thermodynamic and kinetic radii to $3a_0$ and $4a_0$, respectively. This leads to 38 distinct jump frequencies in BCC (78 in FCC); jumps beyond the 2nn shell were set to the isolated vacancy jump frequency. The L_{VV} coefficient is obtained by adding the contribution of the monomers (single vacancies) to that of the OSA-vacancy pair according to Eq. 3, and assuming the pair concentration as $C_{VY} = C_V C_Y Z_{VY}$ ($C_Y = 1\%$). The partition function Z_{VY} is output by KineCluE, while the drag ratios are independent from the vacancy concentration. The results show that Y will diffuse by vacancy drag up to very high temperatures and across the phase transformation to FCC. Therefore, not only the diffusion of Y atoms is faster than Fe self diffusion–as was highlighted by Bocquet–but it is expected that the highly stable split-vacancy complex leads to strong positive (i.e. same direction) flux coupling between Y solutes and vacancies. Note that the values of the L_{VY}/L_{VV} coefficients in Fig. 8 are in principle dependent on the kinetic radius. Indeed, as the kinetic radius increases, more and more V monomer contributions are included in the V-Y pair L_{VV} coefficient. Yet, because there is a strong attractive interaction between V and Y (1.2 eV in BCC and 1.3 eV in FCC), these V monomer contributions are negligible compared with the V-Y pair contribution unless the calculation is performed with a very large kinetic radius.

18

4.2.3. Kick-out and multiple interstitial mechanisms in diamond structures

In semi-conductors with a diamond crystallographic structure, kick-out and multiple interstitial diffusion mechanisms associated with near-value activation energies may contribute to the atomic transport [27]. KineCluE is able to handle these complex diffusion mechanisms. A mechanism frequently invoked is the one combining hops of a dumbbell and direct interstitial (described as the stable-split mechanism in Ref. [83] and as a multiple diffusion mechanism here). The dumbbell is oriented along the $< 110 >$ direction and one of the atoms of the dumbbell is hopping onto a neighboring interstitial site (tetrahedral or hexagonal site). There is also the so-called kick-out mechanism (also called indirect mechanism): an atom sitting on an interstitial site A hops onto a neighboring lattice site B and kicks the substitutional atom which was occupying the lattice site B out onto a neighboring interstitial site C. The interstitial network is either made of tetragonal or hexagonal interstitial sites. For the hexagonal interstitial network, we distinguish three sub-mechanisms depending on the cosine of the angle made between vectors $\vec{AB}$ and $\vec{BC}$: the first sub-mechanism starting from a given site interstitial site A involves two final hexagonal sites C (labeled $(1, 2)$ in [83]) forming a cosine equal to $9/11$, the second sub-mechanism involves two hexagonal sites C labeled $(3, 4)$ forming a cosine equal to $5/11$ and the third set involving four hexagonal sites C labeled $(5, 6, 7, 8)$ forming a cosine equal to $1/11$. The agreement between the correlation factor f_0 obtained from KineCluE and the values extracted from atomic kinetic Monte Carlo simulations [83] is very good for for both the kick-out and multiple diffusion mechanisms. Note that to compare with data from Ref. [83], we have used the measured average cosine value $cos^{tr}\theta$ of the angle between successive jumps of a tracer atom to compute the corresponding f_0 using the formula: $f_0 = 1 + cos^{tr}\theta$. In addition, KineCluE with kinetic radius larger than $20a_0$ has a better precision because the resulting correlation factors are systematically lower than the corresponding Monte Carlo value. The precision of the Monte Carlo simulation is around 10^{-2}, a precision that we get in KineCluE with a kinetic radius approximately equal to $3a$. Thus, although not informed by the authors, we estimate the size of the Monte Carlo simulation box to be around $2 \times 3a_0$. This is based on the idea that kinetic correlations associated with defect trajectories coming out of a Monte Carlo simulation box are not properly taken into account due to the periodic conditions.

4.2.4. Transport coefficients in strained systems

KineCluE allows for a seamless application of the SCMF cluster-expansion method to strained systems, thus widely improving the state-of-the-art models for computing full strain-dependent transport matrices. Strain-dependent diffusion coefficient were measured by molecular dynamics [88] and by Monte Carlo simulations [89], but it was shown that measuring the elasto-diffusion tensor with the latter method is tricky [90]. Previous analytical models allowing for such kind of calculations were based on:

- the SCMF method (before cluster expansion) by Garnier and coworkers for diffusion of substitutional solutes via a vacancy mechanism in FCC alloys [53, 91, 92];

- the Green function method for isolated interstitial solutes and vacancy-solute pairs in any lattice [45, 46].

KineCluE greatly expands the range of systems that can be treated under strain, taking accurately into account all effects on correlations and energetics; for instance, it can correctly describe the effects of strain on the flux coupling between dumbbells and substitutional solutes, for which no model currently exists. In the analytical part code, the symmetry analysis allows for the correct identification of the broken symmetries in the strained crystal, whereas the effect of strain-field elastic energy is automatically included in the numerical code in the framework of linear elasticity theory [75].

The implementation has been successfully tested on the aforementioned studies. Figure 9 shows the drag ratio $L_{\mathrm{BV}}/L_{\mathrm{BB}}$ for a vacancy-solute pair in a FCC model alloy, as a function of different jump frequency ratios in the unstrained crystal (left panel), under a tetragonal strain ε_{33} (middle panel), and under a shear strain $\varepsilon = 2\varepsilon_{12} = 2\varepsilon_{21}$ (right panel). The nomenclature is the same as in the

reference SCMF-based work [92] (Figures 1 and 2 therein). The diffusion direction (e.g. [001]) is controlled in KineCluE with the chemical potential gradient direction, and by optionally adding two other non-collinear diffusion directions in case non-isotropic terms arise. The KineCLuE calculations were performed with a larger kinetic radius ($4a_0$) than Garnier's model ($\sqrt{2}a_0$), which entails larger correlations (larger $|L_{BV}|$) and slower solute diffusion (smaller L_{BB}). Hence, the drag ratios computed with KineCluE are larger in absolute value then the ones computed by Garnier, as shown in Fig. 9. In the example of L_{BV}/L_{BB} [100] under shear strain, atomic kinetic Monte Carlo simulations[92] performed in a $(6a_0)^3$ cell (corresponding approximately to a kinetic radius of $3a_0$) are expected to be located in between the results from KineCluE ($R_{kin} = 4a_0$) and those from Garnier ($R_{kin} = \sqrt{2}a_0$). The fact that they are not is most probably due to statistical uncertainties, especially as the difference appears at large jump frequency ratio.

KineCluE compares well also with the elasto-diffusion calculations performed with the Green Function (GF) method for interstitial carbon diffusion in BCC iron [46]. Figure 10 shows the non-null components of the elasto-diffusion tensor $d_{xy} = dD_{xy}/d\varepsilon$, obtained in KineCluE by finite differences: $d = (L(\varepsilon_1) - L\varepsilon_0)/(\varepsilon_1 - \varepsilon_0)$, with $\varepsilon_0 = 0$ and $\varepsilon_1 = 10^{-6}$. The change of sign of the d_{11} coefficient at $T = 425.1$ K is in perfect agreement with the GF calculations; this has been achieved by setting a sufficiently small $\Delta\varepsilon$. Given that the code is already capable of computing derivatives of the transport coefficients (used for instance in the sensitivity study, cf. Section 4.1.3), it will be possible in future implementations to obtain the exact value of the derivative $dD_{xy}/d\varepsilon$, without the need for finite differences.

5. Conclusion

We introduced the KineCluE code that computes cluster transport coefficients from atomic-scale jump frequencies. The code is highly versatile in terms of crystallographic system, chemical species and defects, interaction ranges, and jump mechanisms, which allows for the treatment of a wide range of systems. It is an important tool to bridge two gaps:

a "scale" gap and a "concentration" gap. For the former, the cluster expansion of the Onsager matrix enables for an efficient evaluation of kinetic properties as functions of cluster concentrations, since cluster transport coefficients only have to be computed once. Coupling with cluster dynamics and phase field methods is thus straightforward, and KineCluE allows to truly link these methods with atomic-scale information such as energies of configurations and migration barriers under well-controlled approximations. Also, cluster quantities are directly useful to object kinetic Monte Carlo methods. In the end, KineCluE offers new possibilities for studying micro-structure and defect population evolution over significant time scales informed by atomic scale data. Regarding the concentration gap, available analytical kinetic models have always been separated into exact models for infinitely dilute systems and mean field approaches for concentrated models. Starting from a dilute system framework, KineCluE allows for the treatment of larger clusters than what has been done previously, and these clusters contain some of the physics of concentration effects on transport properties. Thus, it is a first but important step in unifying both dilute and concentrated approaches in a unique formalism that would be able to correctly describe intermediate concentrations (a few percent) which are probably the most useful but also the most challenging to compute.

Acknowledgments

Appendix: Sensitivity study

Transport coefficients for cluster of more than two components depend on a large number of jump frequencies, and this number increases exponentially with the number of components in the cluster. The sensitivity study is a routine of KineCluE designed to identify the most important jump frequencies by
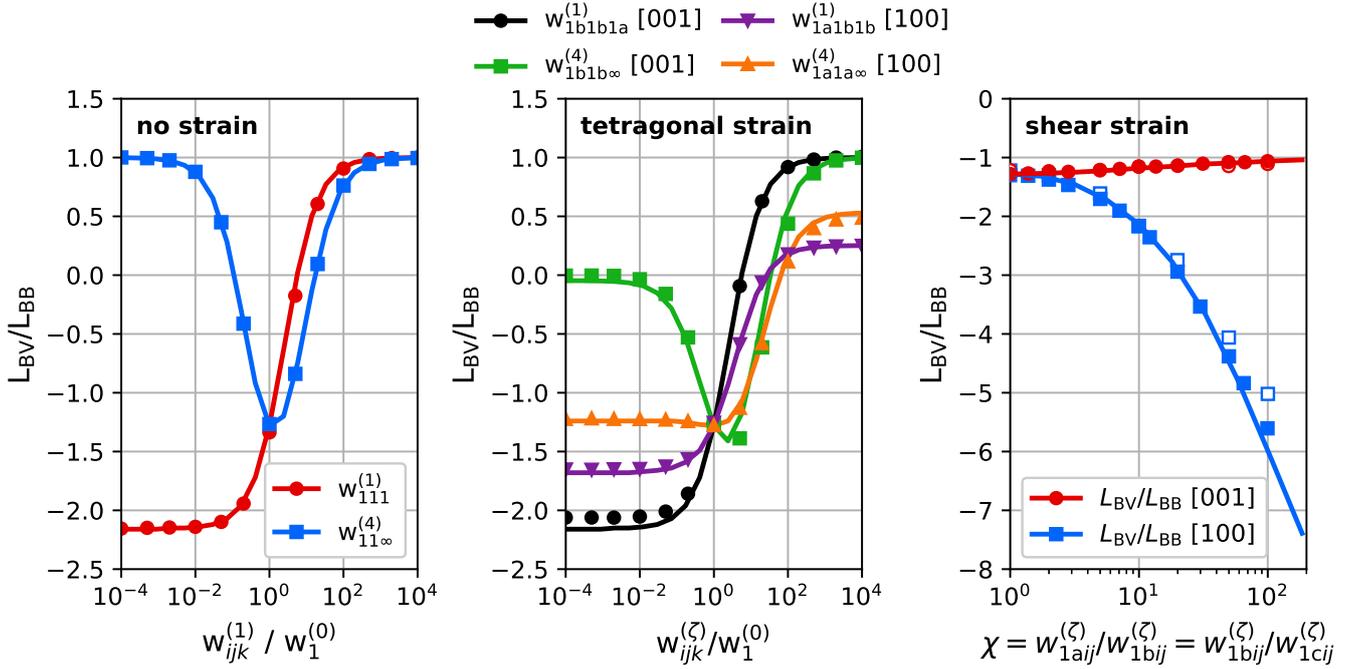
20

Figure 9: Drag ratios for substitutional solute diffusion by vacancies in an FCC model alloy without strain (left), under a tetragonal strain ε_{33} (middle), and under a shear strain (right), as functions of different frequency ratios, compared with the SCMF calculations of a previous work [92] (full markers) and using the nomenclature therein. Empty markers report the corresponding KMC calculations in the same work. Each strain calculation refers to a specific diffusion direction (in the shown cases, directions [100] and [010] are equivalent).
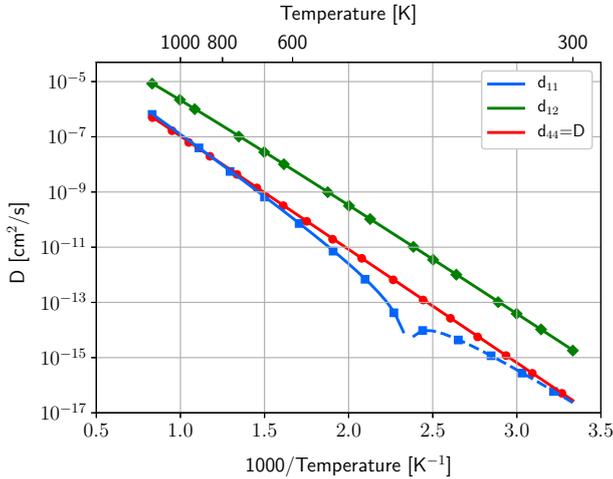
Figure 10: Components of the elasto-diffusion tensor for interstitial carbon diffusion in BCC iron, compared with the Green function method (markers)[46]. In perfect agreement with the reference work, the d_{11} coefficient shows a sign change at T = 425.1 K (negative values are marked with a dashed line), and the d_{44} coefficient is exactly equal to the carbon diffusivity in the unstrained crystal.

computing the local derivatives of cluster transport coefficients with respect to jump frequencies. Starting from a set of jump frequencies–which might not be very accurate–this routine identifies the most critical jump frequencies, i.e. the ones that need to be computed accurately to have reliable transport coefficients. Because the method is only local, several iterations might be necessary to identify the full set of critical jump frequencies.

Let us assume that we have a set of jump frequencies $\mathbf{W}_0 = \left(\omega_i^0\right)$; we are then able to compute a numerical value for $\mathbf{L}_d(\mathbf{W}_0)$. Now we want to know how $\mathbf{L}_d(\mathbf{W}_0)$ would change if some of the jump frequencies ω_i would be modified. To this end, we will compute the gradient of $\mathbf{L}_d$ in the jump frequency phase space which points towards the direction of the highest change in $\mathbf{L}_d$:

$$\boldsymbol{\nabla}\mathbf{L}_d = \left(\left.\frac{\partial\mathbf{L}_d}{\partial\omega_i}\right|_{\mathbf{W}_0}\right). \tag{25}$$

We compute the partial derivatives using the matrix form of cluster transport coefficients: $\mathbf{L}_d(c) = \mathbf{\Lambda}_d^0 -$

$\boldsymbol{\Lambda}_d \tilde{\mathbf{T}}^{-1} \boldsymbol{\Lambda}_\mu^t$ (Eq. 23):

$$\frac{\partial \mathbf{L}_d}{\partial \omega_i} = \frac{\partial \boldsymbol{\Lambda}_d^0}{\partial \omega_i} + \frac{\partial \boldsymbol{\Lambda}_d}{\partial \omega_i} \tilde{\mathbf{T}}^{-1} \boldsymbol{\Lambda}_\mu^t + \boldsymbol{\Lambda}_d \frac{\partial \tilde{\boldsymbol{T}}^{-1}}{\partial \omega_i} \boldsymbol{\Lambda}_\mu^t + \boldsymbol{\Lambda}_d \tilde{\mathbf{T}}^{-1} \frac{\partial \boldsymbol{\Lambda}_\mu^t}{\partial \omega_i}. \tag{26}$$

Note that all the above matrices and derivatives are evaluated at $\mathbf{W}_0$. The terms in matrices $\boldsymbol{\Lambda}^0$, $\boldsymbol{\Lambda}$ and $\tilde{\mathbf{T}}$ are linear combinations of jump frequencies, and we have computed their analytical form in the first part of the KineCluE code, so their derivatives with respect to a given jump frequency ω_i are straightforward to compute. The remaining issue is that we do not have the analytical expression of $\tilde{\mathbf{T}}^{-1}$, and it can be prohibitively long to compute because $\tilde{\mathbf{T}}$ is a square matrix of size the number of effective interactions in the system. Thus, we use the following identity:

$$\tilde{\mathbf{T}} \tilde{\mathbf{T}}^{-1} = \mathbf{I} \Rightarrow \frac{\partial \tilde{\mathbf{T}}}{\partial \omega_i} \tilde{\mathbf{T}}^{-1} + \tilde{\mathbf{T}} \frac{\partial \tilde{\mathbf{T}}^{-1}}{\partial \omega_i} = \mathbf{0}$$

$$\Rightarrow \frac{\partial \tilde{\mathbf{T}}^{-1}}{\partial \omega_i} = -\tilde{\mathbf{T}}^{-1} \frac{\partial \tilde{\mathbf{T}}}{\partial \omega_i} \tilde{\mathbf{T}}^{-1}. \tag{27}$$

Inserting Eq. 27 in Eq. 26 amounts to a practically convenient expression:

$$\frac{\partial \mathbf{L}_d}{\partial \omega_i} = \frac{\partial \boldsymbol{\Lambda}_d^0}{\partial \omega_i} + \frac{\partial \boldsymbol{\Lambda}_d}{\partial \omega_i} \tilde{\mathbf{T}}^{-1} \boldsymbol{\Lambda}_\mu - \boldsymbol{\Lambda}_d \tilde{\mathbf{T}}^{-1} \frac{\partial \tilde{\mathbf{T}}}{\partial \omega_i} \tilde{\mathbf{T}}^{-1} \boldsymbol{\Lambda}_\mu$$

$$+ \boldsymbol{\Lambda}_d \tilde{\mathbf{T}}^{-1} \frac{\partial \boldsymbol{\Lambda}_\mu}{\partial \omega_i}. \tag{28}$$

Now all the derivatives can be easily computed from the analytical expressions of $\boldsymbol{\Lambda}^0$, $\boldsymbol{\Lambda}$ and $\tilde{\mathbf{T}}$. Then, for a given set of jump frequencies $\mathbf{W}_0$, all terms located in Eq. 28 are directly computed numerically, and the numerical value of $\tilde{\mathbf{T}}^{-1}$ is already known from the calculation of $\mathbf{L}_d(\mathbf{W}_0)$. The direction $\mathbf{V}$ in jump frequency space along which $\mathbf{L}_d$ varies the most around $\mathbf{W}_0$ is given by the normalized gradient:

$$\mathbf{V} = \frac{\nabla \mathbf{L}_d}{\|\nabla \mathbf{L}_d\|} = \frac{\nabla \mathbf{L}_d}{\sqrt{\nabla \mathbf{L}_d . \nabla \mathbf{L}_d}}. \tag{29}$$

Practically speaking, vector $\mathbf{V}$ gives the weighted combination of jump frequencies that is able to affect the most $\mathbf{L}_d(\mathbf{W}_0)$. These weights then show which are the most critical jump frequencies to get an accurate estimation of $\mathbf{L}_d$ around $\mathbf{W}_0$. These jump frequencies should be computed accurately (e.g. using

first-principles calculations) to obtain a new estimation of $\mathbf{L}_d$ around a new point in the jump frequency space, $\mathbf{W}_1$. Then again, the corresponding $\mathbf{V}$ vector is obtained to see which are the most relevant jump frequencies around that point, and so on and so forth.

The remaining question is: when should we stop? Because the analysis is only local, when we change some of the jump frequencies, we will not get the same set of critical jump frequencies, and eventually we might end up computing all of these, which we wanted to avoid originally. The idea is to take a set of jump frequencies among the ones with the highest $\mathbf{V}$ vector components and compute the numerical value of transport coefficients for changes in these jump frequency values. A batch calculation feature is provided in KineCluE for this purpose. Then, one can decide if it is worth computing precisely the value of a given saddle-point configuration, or if it does not affect cluster transport coefficients within a tolerance chosen by the user. An example of such procedure is presented in Sec. 4.1.3.

Another possible approach which is not yet part of the KineCluE code, is to compute the Taylor expansion of transport coefficients around a reference point in jump frequency space. This may be numerically advantageous because any order derivative of cluster transport coefficients uses the same derivatives as the gradient, so there is no additional analytical effort needed, it is only a numerical application which requires matrix multiplications. The Nth-order Taylor expansion for multivariate functions reads:

$$\mathbf{L}_d = \sum_{|n|=0}^{N} \prod_{i=0}^{n} \left[\frac{\left(\omega_i - \omega_i^0 \right)^{n_i}}{n_i!} \left. \frac{\partial^{n_i} \mathbf{L}_d}{\partial \omega_i^{n_i}} \right|_{\mathbf{W}_0} \right] \tag{30}$$

where $|n| = k$ denotes a sum over all possible values of $\{n_i\}$ where $\sum_i n_i = k$. The nth order derivative (for $n > 1$) of $\mathbf{L}_d$ with respect to n jump frequencies (eventually some jump frequencies may appear more than once) is expressed as:

$$\frac{\partial^n \mathbf{L}_d}{\partial \omega^n} = \mathbf{\Lambda}_d \frac{\partial^n \tilde{\mathbf{T}}^{-1}}{\partial \omega^n} \mathbf{\Lambda}_\mu^t$$
$$+ \sum_{\gamma=1}^n \left[\frac{\partial \mathbf{\Lambda}_d}{\partial \omega_\gamma} \frac{\partial^{n-1} \tilde{\mathbf{T}}^{-1}}{\partial \omega_{\neq\gamma}^{n-1}} \mathbf{\Lambda}_\mu^t + \mathbf{\Lambda}_d \frac{\partial^{n-1} \tilde{\mathbf{T}}^{-1}}{\partial \omega_{\neq\gamma}^{n-1}} \frac{\partial \mathbf{\Lambda}_\mu^t}{\partial \omega_\gamma} \right]$$
$$+ \sum_{1 \leq \gamma < \delta \leq n} \left[\frac{\partial \mathbf{\Lambda}_d}{\partial \omega_\gamma} \frac{\partial^{n-2} \tilde{\mathbf{T}}^{-1}}{\partial \omega_{\neq\gamma,\delta}^{n-2}} \frac{\partial \mathbf{\Lambda}_\mu^t}{\partial \omega_\delta} + \frac{\partial \mathbf{\Lambda}_d}{\partial \omega_\delta} \frac{\partial^{n-2} \tilde{\mathbf{T}}^{-1}}{\partial \omega_{\neq\gamma,\delta}^{n-2}} \frac{\partial \mathbf{\Lambda}_\mu^t}{\partial \omega_\gamma} \right].$$
$$(31)$$

The nth order derivative of the inverse of the $\tilde{\mathbf{T}}$ matrix is given as:

$$\frac{\partial^n \tilde{\mathbf{T}}^{-1}}{\partial \omega^n} = \left[\sum_\rho \prod_{i=1}^n \left(-\tilde{\mathbf{T}}^{-1} \frac{\partial \tilde{\mathbf{T}}}{\partial \omega_{\rho(i)}} \right) \right] \tilde{\mathbf{T}}^{-1}, \qquad (32)$$

where the sum over ρ denotes a sum over the possible permutations of jump frequencies and a short-hand notation is used in the two previous equations:

$$\frac{\partial^{n-1} A}{\partial \omega_{\neq j}^{n-1}} = \frac{\partial^{n-1} A}{\partial \omega_1 ... \partial \omega_{j-1} \partial \omega_{j+1} ... \partial \omega_n} \qquad (33)$$

This way of computing the local variations of cluster transport coefficients in the jump frequency space might be more efficient from a numerical point of view than re-computing transport coefficients for each values of the most important jump frequencies. If testing shows that this Taylor expansion formalism is more efficient, it will be implemented in future versions of KineCluE.

[1] H. Mehrer (Ed.), Diffusion in Solid Metals and Alloys, Vol. 26 of New Series, Group 3, Springer Verlag, 1990.

[2] A. D. Leclaire, A. B. Lidiard, Liii. correlation effects in diffusion in crystals, The Philosophical Magazine: A Journal of Theoretical Experimental and Applied Physics 1 (6) (1956) 518–527. doi:https://doi.org/10.1080/14786435608238133.
URL https://www.tandfonline.com/doi/abs/10.1080/14786435608238133

[3] A. R. Allnatt, A. B. Lidiard, Atomic Transport in Solids, Cambridge University Press, 1993.

[4] R. M. Martin, Electronic Structure, Basic Theory and Practical Methods, Cambridge University Press, 2004.

[5] E. Meslin, C. C. Fu, A. Barbu, Phys. Rev. B 75 (2007) 094303. doi:10.1103/PhysRevB.75.094303, [link].
URL https://journals.aps.org/prb/abstract/10.1103/PhysRevB.75.094303

[6] L. Messina, M. Nastar, N. Sandberg, P. Olsson, Systematic electronic-structure investigation of substitutional impurity diffusion and flux coupling in bcc iron, Phys. Rev. B 93 (2016) 184302. doi:10.1103/PhysRevB.93.184302.
URL https://link.aps.org/doi/10.1103/PhysRevB.93.184302

[7] G. T. Barkema, N. Mousseau, Event-based relaxation of continuous disordered systems, Phys. Rev. Lett. 77 (1996) 4358–4361. doi:10.1103/PhysRevLett.77.4358.
URL https://link.aps.org/doi/10.1103/PhysRevLett.77.4358

[8] R. Kikuchi, J. Phys. Chem. Solids 20 (1961) 17. doi:https://doi.org/10.1016/0022-3697(61)90133-0, [link].
URL https://www.sciencedirect.com/science/article/pii/0022369761901330

[9] R. Kikuchi, H. Sato, J. Chem. Phys. 53 (1970) 2702. doi:https://doi.org/10.1063/1.1674393, [link].
URL https://aip.scitation.org/doi/abs/10.1063/1.1674393

[10] M. Nastar, V. Barbe, Faraday Discussions 134 (2007) 331. doi:10.1039/B605834E.

[11] V. Barbe, M. Nastar, Phys. Rev. B 76 (2007) 054206. doi:https://doi.org/10.1103/PhysRevB.76.054206, [link].
URL https://journals.aps.org/prb/abstract/10.1103/PhysRevB.76.054206

[12] Z. Erdélyi, M. Pasichnyy, V. Bezpalchuk, J. Tomán, B. Gajdics, A. Gusak, Stochastic kinetic mean field model, Computer Physics Communications 204 (2016) 31 – 37. doi:https://doi.org/10.1016/j.cpc.2016.03.003.
URL http://www.sciencedirect.com/science/article/pii/S0010465516300613

[13] V. G. Vaks, K. Y. Khromov, I. R. Pankratov, V. V. Popov, Statistical theory of diffusion in concentrated bcc and fcc alloys and concentration dependencies of diffusion coefficients in bcc alloys fecu, femn, feni, and fecr, Journal of Experimental and Theoretical Physics 123 (1) (2016) 59–85. doi:10.1134/S1063776116070244.
URL https://doi.org/10.1134/S1063776116070244

[14] V. Barbe, M. Nastar, Phil. Mag. 86 (2006) 1513. doi:https://doi.org/10.1080/14786430500383575, [link].
URL https://www.tandfonline.com/doi/full/10.1080/14786430500383575

[15] J. Bocquet, Exact value of the correlation factor for the divacancy mechanism in fcc crystals: the end of a long quest, Philosophical Magazine 95 (4) (2015) 394–423. doi:10.1080/14786435.2015.1006297.
URL https://doi.org/10.1080/14786435.2015.1006297

[16] G. Mills, H. Jónsson, G. K. Schenter, Surf. Sci. 324 (1995) 305. doi:https://doi.org/10.1016/

`0039-6028(94)00731-4`, [link].
URL `https://www.sciencedirect.com/science/article/pii/0039602894007314`

[17] H. Jónsson, G. Mills, K. W. Jacobsen, Nudged Elastic Band Method for Finding Minimum Energy Paths of Transitions, in: B. J. Berne, G. Ciccotti, D. F. Coker (Eds.), Classical and quantum dynamics in condensed phase simulations, Singapore, 1998, p. 35.

[18] G. Henkelman, B. P. Uberuaga, H. Jónsson, J. Chem. Phys. 113 (2000) 9901–9904. `doi:https://doi.org/10.1063/1.1329672`, [link].
URL `https://aip.scitation.org/doi/10.1063/1.1329672`

[19] M. Mantina, Y. Wang, L. Chen, Z. Liu, C. Wolverton, First principles impurity diffusion coefficients, Acta Materialia 57 (14) (2009) 4102 – 4108. `doi:https://doi.org/10.1016/j.actamat.2009.05.006`.
URL `https://www.sciencedirect.com/science/article/pii/S1359645409003048`

[20] S. Choudhury, L. Barnard, J. Tucker, T. Allen, B. Wirth, M. Asta, D. Morgan, Ab-initio based modeling of diffusion in dilute bcc fe-ni and fe-cr alloys and implications for radiation induced segregation, Journal of Nuclear Materials 411 (1) (2011) 1 – 14. `doi:https://doi.org/10.1016/j.jnucmat.2010.12.231`.
URL `http://www.sciencedirect.com/science/article/pii/S0022311510010664`

[21] H. Wu, A. Lorenson, B. Anderson, L. Witteman, H. Wu, B. Meredig, D. Morgan, Robust fcc solute diffusion predictions from ab-initio machine learning methods, Computational Materials Science 134 (2017) 160 – 165. `doi:https://doi.org/10.1016/j.commatsci.2017.03.052`.
URL `http://www.sciencedirect.com/science/article/pii/S0927025617301738`

[22] R. Agarwal, D. R. Trinkle, Ab initio magnesium-solute transport database using exact diffusion theory, Acta Mater. 150 (2018) 339–350. `doi:https://doi.org/10.1016/j.actamat.2018.03.025`.
URL `https://www.sciencedirect.com/science/article/pii/S1359645418302106`

[23] A. Claisse, T. Schuler, D. A. Lopes, P. Olsson, Transport properties in dilute UN(x) solid solutions (x = Xe, Kr), Phys. Rev. B 94 (2016) 174302. `doi:10.1103/PhysRevB.94.174302`.
URL `https://link.aps.org/doi/10.1103/PhysRevB.94.174302`

[24] T. Schuler, D. A. Lopes, A. Claisse, P. Olsson, Transport properties of c and o in un fuels, Phys. Rev. B 95 (2017) 094117. `doi:10.1103/PhysRevB.95.094117`.
URL `https://link.aps.org/doi/10.1103/PhysRevB.95.094117`

[25] X.-Y. Liu, W. Windl, K. M. Beardmore, M. P. Masquelier, First-principles study of phosphorus diffusion in silicon: Interstitial- and vacancy-mediated diffusion mechanisms, Applied Physics Letters 82 (12) (2003) 1839–1841.

`doi:https://doi.org/10.1063/1.1562342`.
URL `https://aip.scitation.org/doi/10.1063/1.1562342`

[26] D. Caliste, P. Pochet, T. Deutsch, F. Lançon, Germanium diffusion mechanisms in silicon from first principles, Phys. Rev. B 75 (2007) 125203. `doi:10.1103/PhysRevB.75.125203`.
URL `https://link.aps.org/doi/10.1103/PhysRevB.75.125203`

[27] F. Bruneval, Range-separated approach to the rpa correlation applied to the van der waals bond and to diffusion of defects, Phys. Rev. Lett. 108 (2012) 256403. `doi:10.1103/PhysRevLett.108.256403`.
URL `https://link.aps.org/doi/10.1103/PhysRevLett.108.256403`

[28] Y. Yoshida, G. Langouche, Defects and Impurities in Silicon Materials: An Introduction to Atomic-Level Silicon Engineering, Springer, 2016.

[29] K. Kobayashi, S. Yamaoka, K. Sueoka, J. Vanhellemont, Thermal equilibrium concentration of intrinsic point defects in heavily doped silicon crystals - theoretical study of formation energy and formation entropy in area of influence of dopant atoms-, Journal of Crystal Growth 474 (2017) 110 – 120, the 8th International Workshop on Modeling in Crystal Growth. `doi:https://doi.org/10.1016/j.jcrysgro.2016.11.098`.
URL `http://www.sciencedirect.com/science/article/pii/S0022024816308119`

[30] L. Onsager, Phys. Rev. 37 (1931) 405. `doi:https://doi.org/10.1103/PhysRev.37.405`, [link].
URL `https://journals.aps.org/pr/abstract/10.1103/PhysRev.37.405`

[31] M. Nastar, F. Soisson, Comprehensive Nuclear Materials, Vol. 5, Elsevier, Ed. Rudy Konings, 2013. `doi:https://doi.org/10.1016/B978-0-08-056033-5.00035-5`.
URL `https://www.sciencedirect.com/science/article/pii/B9780080560335000355`

[32] A. J. Ardell, P. Bellon, Radiation-induced solute segregation in metallic alloys, Current Opinion in Solid State and Materials Science 20 (3) (2016) 115–139. `doi:10.1016/j.cossms.2015.11.001`.
URL `http://dx.doi.org/10.1016/j.cossms.2015.11.001`

[33] T. R. Anthony, Diffusion in solids, Academic Press, New York, 1975.

[34] M. Zehetbauer, G. Steiner, E. Schafler, A. V. Korznikov, E. Korznikova, Deformation induced vacancies with severe plastic deformation: Measurements and modelling, in: Nanomaterials by Severe Plastic Deformation, Vol. 503 of Materials Science Forum, Trans Tech Publications, 2006, pp. 57–64. `doi:10.4028/www.scientific.net/MSF.503-504.57`.

[35] A. Barbu, Acta Met. 28 (1980) 499. `doi:https://doi.org/10.1016/0001-6160(80)90140-6`, [link].
URL `https://www.sciencedirect.com/science/`

article/pii/0001616080901406

[36] J.-L. Bocquet, Phil. Mag. A 63 (1991) 157. doi:https://doi.org/10.1080/01418619108204843, [link].
URL https://www.tandfonline.com/doi/abs/10.1080/01418619108204843

[37] V. Barbe, M. Nastar, Phil. Mag. 87 (2006) 1649. doi:https://doi.org/10.1080/14786430600917223, [link].
URL https://www.tandfonline.com/doi/abs/10.1080/14786430600917223

[38] T. Garnier, M. Nastar, P. Bellon, D. R. Trinkle, Solute drag by vacancies in body-centered cubic alloys, Phys. Rev. B 88 (2013) 134201. doi:https://doi.org/10.1103/PhysRevB.88.134201.
URL https://journals.aps.org/prb/abstract/10.1103/PhysRevB.88.134201

[39] T. Garnier, D. R. Trinkle, M. Nastar, P. Bellon, Quantitative modeling of solute drag by vacancies in face-centered-cubic alloys, Phys. Rev. B 89 (2014) 144202. doi:https://doi.org/10.1103/PhysRevB.89.144202.
URL https://journals.aps.org/prb/abstract/10.1103/PhysRevB.89.144202

[40] L. Messina, M. Nastar, N. Sandberg, P. Olsson, Systematic electronic-structure investigation of substitutional impurity diffusion and flux coupling in bcc iron, Phys. Rev. B 93 (2016) 184302. doi:10.1103/PhysRevB.93.184302.
URL https://link.aps.org/doi/10.1103/PhysRevB.93.184302

[41] T. Schuler, M. Nastar, Transport properties of dilute $\alpha-$Fe(x) solid solutions (x = c, n, o), Phys. Rev. B 93 (2016) 224101. doi:10.1103/PhysRevB.93.224101.
URL https://link.aps.org/doi/10.1103/PhysRevB.93.224101

[42] T. Schuler, D. R. Trinkle, P. Bellon, R. Averback, Design principles for radiation-resistant solid solutions, Phys. Rev. B 95 (2017) 174102. doi:10.1103/PhysRevB.95.174102.
URL https://link.aps.org/doi/10.1103/PhysRevB.95.174102

[43] R. Agarwal, D. R. Trinkle, Exact model of vacancy-mediated solute transport in magnesium, Phys. Rev. Lett. 118 (2017) 105901. doi:10.1103/PhysRevLett.118.105901.
URL https://link.aps.org/doi/10.1103/PhysRevLett.118.105901

[44] J. Bocquet, Correlation factor for diffusion in cubic crystals with solute-vacancy interactions of arbitrary range, Philosophical Magazine 94 (31) (2014) 3603–3631. doi:10.1080/14786435.2014.965768.
URL https://doi.org/10.1080/14786435.2014.965768

[45] D. R. Trinkle, Automatic numerical evaluation of vacancy-mediated transport for arbitrary crystals: Onsager coefficients in the dilute limit using a green function

approach, Philosophical Magazine 97 (28) (2017) 2514–2563. doi:10.1080/14786435.2017.1340685.
URL https://doi.org/10.1080/14786435.2017.1340685

[46] D. R. Trinkle, Diffusivity and derivatives for interstitial solutes: activation energy, volume, and elastodiffusion tensors, Philosophical Magazine 96 (26) (2016) 2714–2735. doi:10.1080/14786435.2016.1212175.
URL https://doi.org/10.1080/14786435.2016.1212175

[47] C. Kipnis, Scaling Limits of Interacting Particle Systems, Springer-Verlag Berlin, 1999.

[48] H. Spohn, Large Scale Dynamics of Interacting Particles, Springer-Verlag Berlin Heidelberg, 1991.

[49] C. Arita, P. L. Krapivsky, K. Mallick, Bulk diffusion in a kinetically constrained lattice gas, Journal of Physics A: Mathematical and Theoretical 51 (12) (2018) 125002.
URL http://stacks.iop.org/1751-8121/51/i=12/a=125002

[50] M. Nastar, V. Y. Dobretsov, G. Martin, Phil. Mag. A 80 (2000) 155. doi:https://doi.org/10.1080/01418610008212047, [link].
URL https://www.tandfonline.com/doi/abs/10.1080/01418610008212047

[51] M. Nastar, Atomic diffusion theory challenging the cahn-hilliard method, Phys. Rev. B 90 (2014) 144101. doi:10.1103/PhysRevB.90.144101.
URL https://link.aps.org/doi/10.1103/PhysRevB.90.144101

[52] M. Nastar, Philos. Mag. 85 (2005) 3767–3794. doi:https://doi.org/10.1080/14786430500228390, [link].
URL https://www.tandfonline.com/doi/abs/10.1080/14786430500228390

[53] T. Garnier, V. R. Manga, D. R. Trinkle, M. Nastar, P. Bellon, Stress-induced anisotropic diffusion in alloys: Complex si solute flow near a dislocation core in ni, Phys. Rev. B 88 (2013) 134108. doi:https://doi.org/10.1103/PhysRevB.88.134108.
URL https://journals.aps.org/prb/abstract/10.1103/PhysRevB.88.134108

[54] C. C. Fu, F. Willaime, Phys. Rev. B 72 (2005) 064117. doi:https://doi.org/10.1103/PhysRevB.72.064117, [link].
URL https://journals.aps.org/prb/abstract/10.1103/PhysRevB.72.064117

[55] J.-L. Bocquet, C. Barouh, C.-C. Fu, Migration mechanism for oversized solutes in cubic lattices: The case of yttrium in iron, Phys. Rev. B 95 (21) (2017) 214108. doi:https://doi.org/10.1103/PhysRevB.95.214108.
URL https://journals.aps.org/prb/abstract/10.1103/PhysRevB.95.214108

[56] T. Schuler, M. Nastar, On cluster transport coefficients and the local equilibrium hypothesis, In preparation.

[57] L. Onsager, Phys. Rev. 38 (1931) 2265. doi:https://doi.org/10.1103/PhysRev.38.2265, [link].

URL `https://journals.aps.org/pr/abstract/10.1103/PhysRev.38.2265`

[58] A. R. Allnatt, Einstein and linear response formulae for the phenomenological coefficients for isothermal matter transport in solids, Journal of Physics C: Solid State Physics 15 (27) (1982) 5605–5613. `doi:10.1088/0022-3719/15/27/016`.
URL `http://dx.doi.org/10.1088/0022-3719/15/27/016`

[59] A. Vattré, T. Jourdan, H. Ding, M.-C. Marinica, M. J. Demkowicz, Non-random walk diffusion enhances the sink strength of semicoherent interfaces, Nat Comms 7 (2016) 10424. `doi:10.1038/ncomms10424`.
URL `http://dx.doi.org/10.1038/ncomms10424`

[60] L. Messina, M. Chiapetto, P. Olsson, C. S. Becquart, L. Malerba, An object kinetic monte carlo model for the microstructure evolution of neutron-irradiated reactor pressure vessel steels, physica status solidi a 213 (11) (2016) 2974–2980. `doi:https://doi.org/10.1002/pssa.201600038`.
URL `https://onlinelibrary.wiley.com/doi/abs/10.1002/pssa.201600038`

[61] Z. Yang, S. Blondel, K. D. Hammond, B. D. Wirth, Kinetic monte carlo simulations of helium cluster nucleation in tungsten with preexisting vacancies, FUSION SCIENCE AND TECHNOLOGY 71 (1, SI) (2017) 60–74. `doi:10.13182/FST16-111`.

[62] N. Castin, G. Bonny, A. Bakaev, C. J. Ortiz, A. E. Sand, D. Terentyev, Object kinetic monte carlo model for neutron and ion irradiation in tungsten: Impact of transmutation and carbon impurities, JOURNAL OF NUCLEAR MATERIALS 500 (2018) 15–25. `doi:10.1016/j.jnucmat.2017.12.014`.

[63] M. Chiapetto, L. Malerba, C. S. Becquart, Nanostructure evolution under irradiation in femnni alloys: A "grey alloy" object kinetic monte carlo model, JOURNAL OF NUCLEAR MATERIALS 462 (2015) 91–99. `doi:10.1016/j.jnucmat.2015.03.045`.

[64] A. De Backer, G. Adjanor, C. Domain, M. L. Lescoat, S. Jublot-Leclerc, F. Fortuna, A. Gentils, C. J. Ortiz, A. Souidi, C. S. Becquart, Modeling of helium bubble nucleation and growth in austenitic stainless steels using an object kinetic monte carlo method, NUCLEAR INSTRUMENTS & METHODS IN PHYSICS RESEARCH SECTION B-BEAM INTERACTIONS WITH MATERIALS AND ATOMS 352 (2015) 107–114. `doi:10.1016/j.nimb.2014.11.110`.

[65] H. Xu, Y. N. Osetsky, R. E. Stoller, Cascade annealing simulations of bcc iron using object kinetic monte carlo, JOURNAL OF NUCLEAR MATERIALS 423 (1-3) (2012) 102–109. `doi:10.1016/j.jnucmat.2012.01.020`.

[66] T. Jourdan, G. Bencteux, G. Adjanor, Efficient simulation of kinetics of radiation induced defects: A cluster dynamics approach, Journal of Nuclear Materials 444 (1-3) (2014) 298–313.

`doi:10.1016/j.jnucmat.2013.10.009`.
URL `http://dx.doi.org/10.1016/j.jnucmat.2013.10.009`

[67] R. E. Stoller, S. I. Golubov, C. Domain, C. S. Becquart, Mean field rate theory and object kinetic monte carlo: A comparison of kinetic models;, JOURNAL OF NUCLEAR MATERIALS 382 (2-3) (2008) 77–90. `doi:10.1016/j.jnucmat.2008.08.047`.

[68] F. Soisson, T. Jourdan, Radiation-accelerated precipitation in fe-cr alloys, ACTA MATERIALIA 103 (2016) 870–881. `doi:10.1016/j.actamat.2015.11.001`.

[69] E. Clouet, ASM Handbook, volume 22A Fundamentals of Modeling for Metals Processing, ASM International, 2009, Ch. Modeling of Nucleation Processes, pp. 203–219.

[70] A. Badillo, P. Bellon, R. S. Averback, A phase field model for segregation and precipitation induced by irradiation in alloys, Modelling Simul. Mater. Sci. Eng. 23 (3) (2015) 035008. `doi:10.1088/0965-0393/23/3/035008`.
URL `http://dx.doi.org/10.1088/0965-0393/23/3/035008`

[71] J. Piochaud, M. Nastar, F. Soisson, L. Thuinet, A. Legris, Atomic-based phase-field method for the modeling of radiation induced segregation in fe–cr, Computational Materials Science 122 (2016) 249 – 262. `doi:https://doi.org/10.1016/j.commatsci.2016.05.021`.
URL `https://www.sciencedirect.com/science/article/pii/S0927025616302452`

[72] L. Thuinet, M. Nastar, E. Martinez, G. B. Moladje, A. Legris, F. Soisson, Multiscale modeling of radiation induced segregation in iron based alloys, Computational Materials Science 149 (2018) 324 – 335. `doi:https://doi.org/10.1016/j.commatsci.2018.03.024`.
URL `https://www.sciencedirect.com/science/article/pii/S0927025618301770`

[73] L. Messina, Multiscale modeling of atomic transport phenomena in ferritic steels, Ph.D. thesis, KTH Royal Institute of Technology, KTH Royal Institute of Technology (Dec. 2015).

[74] G. Nandipati, N. Govind, A. Andersen, A. Rohatgi, Self-learning kinetic monte carlo simulations of al diffusion in mg, Journal of Physics: Condensed Matter 28 (15) (2016) 155001.
URL `http://stacks.iop.org/0953-8984/28/i=15/a=155001`

[75] C. Varvenne, F. Bruneval, M.-C. Marinica, E. Clouet, Point defect modeling in materials: Coupling ab initio and elasticity approaches, Phys. Rev. B 88 (13) (2013) 134102. `doi:https://doi.org/10.1103/PhysRevB.88.134102`.
URL `https://journals.aps.org/prb/abstract/10.1103/PhysRevB.88.134102`

[76] T. Schuler, L. Messina, M. Nastar, Kineclue repository.
URL `http://www...`

[77] C. Barouh, T. Schuler, C.-C. Fu, T. Jourdan, Physical Review B 92 (10). `doi:10.1103/PhysRevB.92.104102`,

[link].
URL https://journals.aps.org/prb/abstract/10.1103/PhysRevB.92.104102

[78] A. Van der Ven, G. Ceder, First principles calculation of the interdiffusion coefficient in binary alloys, Physical Review Letters 94 (4) (2005) 045901. doi:10.1103/physrevlett.94.045901.
URL http://dx.doi.org/10.1103/PhysRevLett.94.045901

[79] J.-L. Bocquet, Phil. Mag. A 47 (1983) 547–577. doi:https://doi.org/10.1080/01418618308245246, [link].
URL https://www.tandfonline.com/doi/abs/10.1080/01418618308245246

[80] P. Benoist, J.-L. Bocquet, P. Lafore, La correlation entre sauts atomiques: Une nouvelle methode de calcul, Acta Metallurgica 25 (3) (1977) 265 – 275. doi:https://doi.org/10.1016/0001-6160(77)90145-6.
URL http://www.sciencedirect.com/science/article/pii/0001616077901456

[81] J. R. Manning, Phys. Rev. B 136 (1964) A1758–A1766. doi:https://doi.org/10.1103/PhysRev.136.A1758, [link].
URL https://journals.aps.org/pr/abstract/10.1103/PhysRev.136.A1758

[82] K. Compaan, Y. Haven, Correlation factors for diffusion in solids, Transactions of the Faraday Society 52 (1956) 786–801. doi:10.1039/TF9565200786.

[83] R. Chen, S. T. Dunham, Correlation factors for interstitial-mediated self-diffusion in the diamond lattice: Kinetic lattice monte carlo approach, Phys. Rev. B 83 (2011) 134124. doi:10.1103/PhysRevB.83.134124.
URL https://link.aps.org/doi/10.1103/PhysRevB.83.134124

[84] S. Ishioka, M. Koiwa, Philos. Mag. A 37 (1978) 517–533. doi:https://doi.org/10.1080/01418617808239187, [link].
URL https://www.tandfonline.com/doi/abs/10.1080/01418617808239187

[85] M. Koiwa, S. Ishioka, Philos. Mag. A 47 (1983) 927–938. doi:https://doi.org/10.1080/01418618308243130, [link].
URL https://www.tandfonline.com/doi/abs/10.1080/01418618308243130

[86] K. Compaan, Y. Haven, Correlation factors for diffusion in solids. part 2.-indirect interstitial mechanism, Trans. Faraday Soc. 54 (1958) 1498–1508. doi:10.1039/TF9585401498.
URL http://dx.doi.org/10.1039/TF9585401498

[87] R. Siegel, Point defects and defect interactions in metals, in: Proc. of Yamada Conf. V, University of Tokyo Press, 1982, p. 533.

[88] W.-L. Chan, R. S. Averback, Y. Ashkenazy, Anisotropic diffusion of point defects in metals under a biaxial stress field simulation and theory, Journal of Applied Physics 104 (2) (2008) 023502. doi:10.1063/1.2955786.
URL https://doi.org/10.1063/1.2955786

[89] B. Ziebarth, M. Mrovec, C. Elsässer, P. Gumbsch, Influence of dislocation strain fields on the diffusion of interstitial iron impurities in silicon, Phys. Rev. B 92 (2015) 115309. doi:10.1103/PhysRevB.92.115309.
URL https://link.aps.org/doi/10.1103/PhysRevB.92.115309

[90] Z. Li, D. R. Trinkle, Kinetic monte carlo investigation of tetragonal strain on onsager matrices, Phys. Rev. E 93 (2016) 053305. doi:10.1103/PhysRevE.93.053305.
URL https://link.aps.org/doi/10.1103/PhysRevE.93.053305

[91] T. Garnier, V. R. Manga, P. Bellon, D. R. Trinkle, Diffusion of si impurities in ni under stress: A first-principles study, Phys. Rev. B 90 (2014) 024306. doi:10.1103/PhysRevB.90.024306.
URL https://link.aps.org/doi/10.1103/PhysRevB.90.024306

[92] T. Garnier, Z. Li, P. Bellon, D. R. Trinkle, Calculation of strain effects on vacancy-mediated diffusion of impurities in fcc structures: General approach and application to ni1-xsix, Phys. Rev. B 90 (18) (2014) 184301. doi:https://doi.org/10.1103/PhysRevB.90.184301.
URL https://journals.aps.org/prb/abstract/10.1103/PhysRevB.90.184301